

# Core excitations and ionizations of uranyl in $\text{Cs}_2\text{UO}_2\text{Cl}_4$ from relativistic embedded damped response time-dependent density functional theory and equation of motion coupled cluster calculations

Wilken Aldair Misael<sup>a)</sup> and André Severo Pereira Gomes<sup>b)</sup>

*Univ. Lille, CNRS, UMR 8523-PhLAM-Physique des Lasers Atomes et Molécules, F-59000 Lille, France*

(Dated: 21 February 2023)

X-ray spectroscopies, by their high selectivity and sensitivity to the chemical environment around the atoms probed, provide significant insight into the electronic structure of molecules and materials. Interpreting experimental results requires reliable theoretical models, accounting for environment, relativistic, electron correlation, and orbital relaxation effects in a balanced manner. In this work, following up on prior work for valence processes [A. S. P. Gomes *et al.*, Phys. Chem. Chem. Phys. **15**, 15153 (2013)], we present a protocol for the simulation of core excited spectra (with damped response time-dependent density functional theory, 4c-DR-TD-DFT) and ionization energies (with the core-valence separated equation of motion coupled cluster theory, 4c-CVS-EOM-IP) based on the Dirac-Coulomb Hamiltonian, while environment effects are accounted for through the frozen density embedding (FDE) method. We showcase this approach for the uranium  $M_4$ ,  $L_3$ -edge and oxygen K-edge of uranyl tetrachloride  $\text{UO}_2\text{Cl}_4^{2-}$  in a host  $\text{Cs}_2\text{UO}_2\text{Cl}_4$  crystal. We have found that the 4c-DR-TD-DFT simulations yield excitation spectra that very closely match the experiment for the uranium  $M_4$  and oxygen K-edges, with good agreement for the broad experimental spectra for the  $L_3$ -edge. By investigating the sensitivity of spectral shapes to the lifetimes, and by decomposing each peak into its components, we have been able to correlate our results with angle-resolved spectra. We have observed that for the uranium  $M_4$  edge, a simplified model for uranyl tetrachloride – in which an embedding potential replaces the chloride equatorial ligands – closely matches the spectral profile obtained for the uranyl tetrachloride system.

## I. INTRODUCTION

Actinides are relevant to modern societies, first and foremost due to their central role in the nuclear industry<sup>14,15,46,70,125</sup>, and the potentially harmful effects that can occur with their release in the biosphere in the case of industrial accidents<sup>17,37,72,88</sup>. In more recent years, the peculiar properties of materials containing actinides have also spurred interest from both a fundamental perspective as well as for industrial applications in catalysis<sup>18,45,64</sup>, materials<sup>2,52,64,86,121</sup> and nanotechnology<sup>6,49,84,144</sup>.

As these properties stem from subtle differences in the electronic structure of different compounds<sup>21,68,103,138</sup>, a key objective in actinide science is to characterize their electronic structure under different conditions. To this end, spectroscopies involving core electrons<sup>33,50,113,114,122</sup> are particularly interesting since they are very sensitive to changes in oxidation state and on the local chemical environment of the actinides<sup>62,92,133,135,143</sup>.

In recent years, with the development of high-energy fourth-generation synchrotron radiation facilities around the world and the availability of X-ray Free Electron

Lasers (XFELs)<sup>65,114,122</sup>, one has witnessed the development and applications of High-Energy Resolution X-ray Spectroscopy (HERXS) to actinides<sup>10,47,99,102,107,147</sup>.

The set of HERXS techniques includes spectroscopies such as High-Energy Resolution Fluorescence Detected X-ray Absorption Near Edge Structure (HERFD-XANES), High-Energy Resolution Auger Detection (HERAD-XANES), High-Energy X-ray Scattering (HEXS) and Extended X-ray Absorption Fine Structure (EXAFS)<sup>10,45,47,61,62,131</sup>. For actinides, a particularly appealing feature of HERXS measurements is their larger penetration depth, which allows for smaller samples<sup>10,50,102,107,141,147</sup>, this way minimizing the need for extensive radiation exposure protection measures. These experiments also offer increased sensitivity in probing processes that involve transitions to and from  $d$  and  $f$  orbitals, with the latter playing a pivotal role in actinide bonding<sup>31,32,71,75,132,134</sup>.

These experimental developments, and the inherent complexities of interpreting the data generated, have stimulated the use of accurate molecular electronic structure methods as a means to interpret, predict and suggest new measurements in the X-ray range<sup>5,78,104,126,137,146</sup>. While it has long been established that in this regime theoretical approaches must properly account for electron correlation<sup>66,77,85,110,137,146</sup> and orbital relaxation<sup>38,60,89,104,127</sup> in order to yield reliable results, the importance of relativistic effects<sup>26,67,93,98,100</sup>, indispensable for heavy elements, is now also recognized for elements as light as those in the second row of the peri-

<sup>a)</sup>Electronic mail: wilken.misael@univ-lille.fr

<sup>b)</sup>Author to whom correspondence should be addressed; Electronic mail: andre.gomes@univ-lille.fr

odic table. For the core states of heavy elements, incorporating quantum electrodynamics effects (QED), such as vacuum polarization and self-energy, may also be essential to bring calculations into agreement with experiment<sup>28,109,111,120</sup>, in particular for K, L and M edges<sup>58</sup>.

Since most measurements of core spectra are not done for molecules in the gas phase, it may become necessary to include effects from the environment in the calculations. This can be done in an efficient and accurate manner with embedding approaches<sup>34,51,53,117</sup>, whereby a sufficiently accurate fully quantum mechanical (QM) description is applied to the region of interest and a significant portion of the system is represented via quantum (QM/QM) or classically-derived (QM/MM) effective operators, without any *a priori* assumptions on the nature of the region of interest or the environment—which makes them potentially more flexible than other proven approaches based on e.g. explicit and continuum (implicit) solvation models<sup>22,81,82,87</sup> and ligand field theory<sup>9,54,118</sup>.

Among actinides, a particularly important class of complexes contains the uranyl ( $\text{UO}_2^{n+}$ ,  $n = 1, 2$ ) moiety, which is ubiquitous in the solution and solid-state chemistry of uranium. It is known to show very strong U-O triple bonds<sup>21</sup> and generally presents a linear O-U-O geometry, with other ligands coordinating to uranium at the equatorial plane, via less strong interactions. The core spectroscopy of uranyl coordination complexes has been investigated with several theoretical methods, ranging from complete and restricted active space self-consistent field<sup>31,91,96,105,106</sup>, crystal ligand-field multiplet theory and its variations<sup>9,48,61,94,95,119,133</sup>, density functional theory in its different flavors<sup>57,61,73,90,110,132</sup>, self-consistent real-space multiple scattering<sup>61,131</sup>, static exchange approximation<sup>110</sup> and perturbation theory<sup>110</sup>.

For molecular-based approaches, relativistic correlated many-body approaches<sup>39,91,105</sup> are among the most accurate approaches that can be used, but their relatively high computational cost makes it difficult to employ for the experimentally relevant systems in the condensed phase. In the case of absorption spectroscopy, it has been found that with a suitable choice of density functional approximation (DFA) – notably the CAM-B3LYP functional<sup>142</sup> – density functional theory (DFT) can provide reliable excitation energies of actinides in the ultraviolet-visible region<sup>35,81–83,97,116</sup>, with a recent, very comprehensive work by Konecny *et al.*<sup>57</sup> employing the four component Damped Response Time-Dependent Density Functional Theory (4c-DR-TD-DFT) formalism, indicating that the same holds for core excited states of uranium complexes.

One aspect that, in our view, was not sufficiently addressed in the work by Konecny and co-workers, is the extent to which the environment can play a role in the spectral features. Furthermore, while there is a comparison between theory and experiment for the uranium  $\text{M}_4$  edge of uranyl bis-nitrate anion ( $\text{UO}_2(\text{NO}_3)_2^-$ ), there are other systems such as the  $\text{Cs}_2\text{UO}_2\text{Cl}_4$  crystal, for which there are HERFD-XANES spectra for the uranium  $\text{M}_4$

as well as XANES spectra for the uranium  $\text{L}_3$ <sup>132</sup>, and oxygen K edge<sup>19</sup>, which could provide additional comparisons to experiment.

The present work, therefore, aims to employ embedding approaches and the 4c-DR-TD-DFT formalism to investigate the effect of the equatorial chloride ligands bound to the equatorial plane of uranyl in the  $\text{Cs}_2\text{UO}_2\text{Cl}_4$  crystal, on the oxygen K-edge and uranium  $\text{M}_4$ - and  $\text{L}_3$ -edges excited states, with a detailed comparison to experimental results available in the literature for this system. We shall also compare our 4c-DR-TD-DFT results to those obtained with 2-component Hamiltonians such as the eXact 2-Component (X2C)<sup>23</sup> in the Tamm-Dancoff approximation (TDA)<sup>42</sup>. Finally, in following up on our previous work on low-lying valence excited states<sup>35</sup>, in addition to core excited states, we also investigate the use of embedding models to obtain the corresponding core ionization energies with the Core-Valence Equation-of-Motion Coupled-Cluster Singles and Doubles (CVS-EOM-IP-CCSD) method<sup>39</sup>.

The structure of this article is as follows. In Section II we present a brief overview of the theoretical methods employed in this work. Section III presents the computational details from our calculations. In Section IV we present our results for the simulated X-ray absorption spectra and ionization energies. Finally, in Section V we present our conclusions and some future perspectives.

## II. THEORY

### A. Damped-Response Theory

The presence of a time-dependent external electric field with particular field strength  $F(t)$  may induce electronic transitions in a molecular system.

Within the electric-dipole approximation the coupling between the electric dipole of the system ( $\vec{\mu}$ ) and this external electric field produces the features observed in a spectrum. This way, perturbations on a system can be theoretically tracked by following the contribution of non-zero order terms on the field expansion of the time-dependent polarization:

$$\mu(t) = \mu^0 + \alpha F(t) + \frac{1}{2}\beta F^2(t) + \dots \quad (1)$$

where  $\mu^0$  denotes the permanent electric-dipole moment,  $\alpha$  is the polarizability tensor, and  $\beta$  is the first-order contribution to non-linear processes such as two-photon absorption (TPA).

Within the framework of standard response theory, one-photon absorption processes can be studied by the computation of the resonant-divergent linear response function. In the exact theory case, the response function relating to the electric-dipole polarizability tensor

can be expressed as a sum over states,

$$\alpha_{ij}(\omega) = -\frac{1}{\hbar} \sum_{n>0} \left[ \frac{\langle 0|\hat{\mu}_i|n\rangle \langle n|\hat{\mu}_j|0\rangle}{\omega_{0n} - \omega} + \frac{\langle 0|\hat{\mu}_i|n\rangle \langle n|\hat{\mu}_j|0\rangle}{\omega_{0n} + \omega} \right] \quad (2)$$

where  $\hat{\mu}_i$  corresponds to a component of the electric-dipole operator along a particular direction, and  $\omega_{0n}$  denote the frequency associated with a transition between the ground state ( $|0\rangle$ ) and an excited state ( $|n\rangle$ ), and  $\omega$  the frequency of the perturbing field.

In the approximate case, one generally refrains from using a sum over states expression but rather recasts the determination of the response functions in terms of the iterative solution of response equations and the subsequent assembly of the response functions. From the linear response function, one obtains the excitation energies from the poles of the response function (i.e. when the perturbing frequency matches the one corresponding) while transition moments are obtained from the residues of the response function<sup>12,40,55,76,78,79</sup>.

What Eq. 2 misses, however, is accounting for the relaxation processes that yield finite lifetimes for the different excited states. Such relaxation can be incorporated into theoretical models in a phenomenological way by including damping terms  $\gamma_{0n} = 1/\tau_n$  in the desired response function, where  $\tau_n$  denote the finite lifetime a particular excited state<sup>76,78</sup>. In this case, we have a redefinition in the denominator in Eq. 2 such that

$$\omega_{0n} \rightarrow \omega_{0n} \pm i\gamma_{0n} \quad (3)$$

resulting in a polarizability tensor that becomes a complex quantity. This case is thus referred to as damped-response (DR) theory, for which implementations with relativistic (4- or 2-component) have been presented for mean-field approaches such as DFT by Villaume, Saue, and Norman<sup>128</sup>—which is the implementation used in this work for all excitation energy calculations—and more recently by Konecny *et al.*<sup>56</sup> and Konecny *et al.*<sup>57</sup>.

Considering a randomly oriented molecular sample, the damped response absorption cross section is now written in terms of the isotropic average of the complex component of the polarizability

$$\sigma(\omega) = \frac{\omega}{3\varepsilon_0 c} \Im[(\alpha_{xx}(\omega) + \alpha_{yy}(\omega) + \alpha_{zz}(\omega))] \quad (4)$$

As damped-response theory provides a resonant-convergent expression for the electric-dipole polarizability, one may perform a series of simulations across a range of selected polarizabilities around a resonance, and then extract a theoretical spectrum that contains information on the relaxation process, avoiding the need to introduce artificial broadening.

As previously suggested by Fransson *et al.*<sup>29</sup>, the inclusion of a channel-restriction scheme in simulations of light-matter interaction in the X-ray range may circumvent the presence of undesired features due to the incompleteness of the basis set and the consequent discretization of the continuum. We also point out that

any channel restriction can ease this type of simulation at high energy ranges, as the diagonalization procedure may become computationally infeasible when one includes all possible excitations on these. Thus, the results presented in section IV A were obtained employing a projection-based method, named restricted-excitation-window (REW), whereas one restricts excitations to only those in which the selected orbitals are involved, avoiding features from outer-electrons<sup>4,5,112,145</sup>.

## B. Equation of Motion Coupled-Cluster

Apart from a response theory-based treatment, we can obtain information beyond the ground state by solving wave equations for both the ground and excited states of interest. One such approach is the equation-of-motion coupled-cluster singles doubles (EOM-CCSD) method, in which excited or ionized states (and associated energies) are obtained from

$$\hat{H}|R_\mu\rangle = \Delta E_\mu|R_\mu\rangle, \quad (5)$$

where  $\Delta E_\mu$  denotes the energy difference between a target state  $\mu$  and the ground-state,

$$|R_\mu\rangle = \hat{R}_\mu|\Psi_{CC}\rangle \quad (6)$$

represents the excited state wavefunction, constructed from a wave operator  $\hat{R}_\mu$  acting upon the ground-state coupled cluster wavefunction

$$|\Psi_{CC}\rangle = e^{\hat{T}}|\Phi_0\rangle, \quad (7)$$

$|\Phi_0\rangle$  denoting the (Hartree-Fock) reference wavefunction,  $\hat{T} = \sum_\nu t_\nu \hat{\tau}_\nu$  the cluster operator, and  $\hat{\tau}_\nu$  an excitation operator generating the singly or doubly excited determinant  $|\nu\rangle$  from the reference.

From Eq. 5, we note that the problem of obtaining excited and ionized states in EOM-CC boils down to the diagonalization of the similarity-transformed Hamiltonian,  $\hat{\bar{H}} = e^{-\hat{T}}\hat{H}e^{\hat{T}}$ , within a selected excitation manifold given by the wave operator. Here, we will employ EOM-CC for obtaining ionization energies (EOM-IP-CCSD), and the wave operator takes the form (in second quantization):

$$\hat{R} \equiv \hat{R}^{IP} = \sum_i r_i \{a_i\} + \sum_{i>j,a} r_{ij}^a \{a_i^\dagger a_j a_i\}, \quad (8)$$

with the amplitudes,  $r_i$  representing singly ionized configurations and  $r_{ij}^a$  single ionizations accompanied by relaxation, referred to in the following as the single and double manifolds respectively. Here  $i, j, k \dots$  denote occupied and  $a, b, c \dots$  virtual orbitals/spinors.

In order to target core ionized states, we employ the core-valence separation (CVS) approximation<sup>13,39,41,126,127</sup>, whereby we apply projector operators to Eq. 5 to remove contributions from valence states

(CVS-EOM-IP-CCSD). As discussed by Halbert *et al.*<sup>39</sup>, the CVS approximation is in spirit equivalent to the REW approach employed for the DR-TD-DFT calculations.

### C. Frozen Density Embedding

In the frozen density embedding (FDE) approach<sup>34,51,139,140</sup> one recast DFT into a subsystem theory so that a given system can be partitioned into (at least) two distinct fragments—the active system, or subsystem  $I$  (here a uranyl unit) and the environment or subsystem  $II$  (the rest of the system, e.g. equatorial ligands). The total system's electron density is therefore rewritten as

$$\rho_{total}(\mathbf{r}) = \rho_I(\mathbf{r}) + \rho_{II}(\mathbf{r}) \quad (9)$$

while the energy

$$E_{tot}[\rho_I, \rho_{II}] = E_I[\rho_I] + E_{II}[\rho_{II}] + E_{int}[\rho_I, \rho_{II}] \quad (10)$$

is decomposed into subsystem energies ( $E_i[\rho_i]$ ;  $i = I, II$ ) and interaction term  $E_{int}[\rho_I, \rho_{II}]$ ,

$$\begin{aligned} E_{int}[\rho_I, \rho_{II}] = & \int \rho_I(\mathbf{r}) v_{nuc}^{II}(\mathbf{r}) d^3r + \int \rho_{II}(\mathbf{r}) v_{nuc}^I(\mathbf{r}) d^3r \\ & + E_{nuc}^{I,II} + \iint \frac{\rho_I(\mathbf{r}) \rho_{II}(\mathbf{r}')}{|\mathbf{r} - \mathbf{r}'|} d^3r d^3r' \\ & + E_{xc}^{nadd}[\rho_I, \rho_{II}] + T_s^{nadd}[\rho_I, \rho_{II}] \end{aligned} \quad (11)$$

where  $v_{nuc}^i$  denotes the nuclear potential associated with the atoms in  $i$ -th subsystem,  $E_{xc}^{nadd}$  and  $T_s^{nadd}$  are respectively the non-addictive exchange correlation and kinetic energy.

If all subsystems are treated at the Kohn-Sham DFT level, the individual subsystem energies  $E_i[\rho_i]$  will be the same as those for the DFT formalism, and from minimization of the total energy (Eq. 10) with respect to  $\rho_I$  for a given (frozen)  $\rho_{II}$  one can obtain the orbitals for subsystem  $I$  by solving a set of Kohn-Sham-like equations

$$\left[ -\frac{\nabla^2}{2} + v_{eff}^{KS}[\rho_I](\mathbf{r}) + v_{emb}^I[\rho_I, \rho_{II}](\mathbf{r}) \right] \phi_k^I(\mathbf{r}) = \varepsilon_k^I \phi_k^I(\mathbf{r}) \quad (12)$$

so that in the ground state the different subsystems are coupled to each other through the so-called embedding potential  $v_{emb}^I$ ,

$$\begin{aligned} v_{emb}^I[\rho_I, \rho_{II}](\mathbf{r}) = & \frac{\delta E_{int}[\rho_I, \rho_{II}]}{\delta \rho_I(\mathbf{r})} = v_{nuc}^{II}(\mathbf{r}) + \\ & \int \frac{\rho_{II}(\mathbf{r}') d^3r'}{|\mathbf{r} - \mathbf{r}'|} + \frac{\delta E_{xc}^{nadd}[\rho_I, \rho_{II}]}{\delta \rho_I(\mathbf{r})} + \frac{\delta T_s^{nadd}[\rho_I, \rho_{II}]}{\delta \rho_I(\mathbf{r})} \end{aligned} \quad (13)$$

One can also optimize  $\rho_{II}$ , for instance via the so-called freeze-and-thaw procedure in which the roles of  $\rho_I$  and

$\rho_{II}$  are exchanged when solving Eq. 12. We found this to be particularly important for charged subsystems<sup>7,16,36</sup>.

In the case of a coupled cluster treatment of subsystem  $I$ , we can recast the equations above into a constrained optimization involving Lagrange multipliers<sup>44</sup> in which we arrive at the same expression for the embedding potential in Eq. 13, but formally involving  $\rho_I$  obtained with coupled cluster theory. However, since in order to obtain coupled cluster densities it is necessary to solve both  $T$  and  $\Lambda$  equations, more approximated schemes employing only DFT densities have been put forward<sup>7,36,43</sup> and show very good performance at a much reduced computational cost. In the latter case, the DFT-in-DFT  $v_{emb}$  is simply included as an additional one-electron operator to the Fock matrix in the correlated calculation<sup>36</sup>.

### III. COMPUTATIONAL DETAILS

DR-TD-DFT and CVS-EOM-IP-CCSD calculations, and the corresponding DR-TD-DFT-in-DFT and CVS-EOM-IP-CCSD-in-DFT calculations were performed in DIRAC22<sup>1</sup> version of the DIRAC electronic structure code<sup>101</sup>, as well as development snapshots (34fbd49, 4b35e48, d70bbe283, e061718, e0617189f6, e7e2094). We employed Dyal's all-electron basis sets of double and triple-zeta quality<sup>24,25</sup> for uranium and Dunning's cc-pVTZ basis set<sup>20</sup> for all other atoms. These basis sets were left uncontracted. We have employed a gaussian nuclear model in all calculations<sup>130</sup>.

For all DFT calculations with DIRAC, we have employed the Dirac-Coulomb (<sup>4</sup>DC) Hamiltonian and the long-range corrected CAM-B3LYP<sup>142</sup>, whereas for EOM calculations, we have employed the X2Cmmf<sup>108</sup> Hamiltonian (<sup>2</sup>DC<sup>M</sup>), in which the decoupling of the large and small components is done by block diagonalized the converged 4-component Fock matrix at the end of the SCF procedure. In benchmark calculations with EOM-IP-CCSD, we have also employed the X2Cmmf-Gaunt<sup>108</sup> Hamiltonian (<sup>2</sup>DCG<sup>M</sup>), in which the Gaunt integrals are included in the construction of the (4-component) Fock matrix the SCF step, but are not explicitly included in the transformation from atomic to molecular basis. Apart from the case of CVS-EOM-IP calculations on the bare uranyl ion, we replaced the contributions from ( $SS|SS$ )-type integrals by a simple Coulombic correction<sup>129</sup> for reasons of computational cost.

In all of our calculations, the structures employed were based on the experimental crystal structure of Cs<sub>2</sub>UO<sub>2</sub>Cl<sub>4</sub> reported by Watkin, Denning, and Prout<sup>136</sup>, whose U-O and U-Cl bond lengths are 1.774 Å and 2.673 Å respectively. For the embedding calculations, we employed the same structural models and subsystem partitioning as outlined by Gomes *et al.*<sup>35</sup>. All calculations on the bare uranyl and uranyl tetrachloride were carried out in  $D_{\infty h}$  and  $D_{2h}$  symmetry, respectively, while for embedded uranyl simulations the crystalline site symme-

try ( $C_{2h}$ ) was used.

The embedding potentials employed here were obtained from freeze-thaw calculations employing the scalar-relativistic ZORA Hamiltonian<sup>124</sup>, TZ2P basis sets, the PW91k kinetic energy<sup>8</sup>, the PBE exchange-correlation functional<sup>27</sup> for the non-additive terms and subsystem energies. These calculations were carried out via the PyADF scripting framework<sup>7</sup> and the embedding potentials were subsequently imported into the DIRAC calculations.

For the DR-TD-DFT calculations we selected a frequency range that covered the energy ranges bracketing the main features in the oxygen K edge ( $18.74 - 18.82 E_h$ ) and the uranium  $M_4$  and  $L_3$  absorption edges ( $135.460 - 135.538 E_h$  and  $627.58 - 627.66 E_h$ , respectively). Given the expected shift in these simulations, the first frequency for each interval was obtained by means of the restricted window scheme (REW-TD-DFT)<sup>145</sup> implementation on DIRAC.

In addition to the calculations with DIRAC, for the uranyl tetrachloride dianion species we have carried out standard (without embedding) TD-DFT calculations with the X2C Hamiltonian (including spin-orbit coupling), triple-zeta basis functions with two polarization functions (TZ2P)<sup>123</sup>, and the CAMB3LYP functional with the Amsterdam Density Functional (ADF) software package<sup>115</sup>. As DR-TD-DFT calculations including spin-orbit coupling could not be carried out with ADF, we employed REW-TD-DFT calculations to target the core excited states of interest and employed the Tamm-Dancoff approximation (TDA)<sup>42</sup>, as it yielded spectra of the same quality as standard TD-DFT calculations at a lower computational cost.

From these REW-TD-DFT calculations, we obtained natural transition orbitals (NTOs)<sup>69</sup>, which we used to provide a qualitative analysis of the changes to the electronic structure involved in the core excitations, due to the lack of equivalent functionality in DIRAC.

In selected calculation we accounted for the Breit and QED effects on the uranium orbital energies through atomic corrections based on the work of Koziol and Aucar<sup>58</sup>, as done elsewhere in the literature<sup>39,111</sup>. Since these are not available for uranium, we obtained values by interpolation. Furthermore, for CVS-EOM-IP calculations, we accounted for shifts in binding energies due to the remainder of the crystal environment by applying a constant shift of 6 eV to all energies as determined in<sup>35</sup>.

The data corresponding to the results in this paper are available at the Zenodo repository<sup>74</sup>.

## IV. RESULTS AND DISCUSSION

### A. Photoabsorption

In the following section we present the theoretical absorption spectra at the oxygen K-edge and uranium  $M_4$ - and  $L_3$ -edges of the uranyl tetrachloride dianion

( $UO_2Cl_4^{2-}$ ), a model in which the chloride ions bound to the equatorial plane of the uranyl ion ( $UO_2^{2+}$ ) are represented by a FDE embedding potential ( $UO_2^{2+} @ Cl_4^{4-}$ ), and the uranyl ion without any chloride ligands (respectively structures **b**, **c** and **d** in Figure 1).

Before discussing the relative performance of these different models, we focus on the spectral shapes obtained from the DR-TD-DFT calculations, and on the analysis of the transitions for each edge on the basis of NTOs.

### 1. Features in the X-ray absorption spectra

The absorption spectrum of the  $Cs_2UO_2Cl_4$  crystal has been utilized in multiple studies as a tool to examine the electric properties of the uranyl(VI) ion in diverse environments, including one- and two-photon absorption at visible light<sup>3,20</sup>. The X-ray Absorption Near Edge Structure (XANES) spectrum at the oxygen K-edge of  $Cs_2UO_2Cl_4$  was first reported by Denning *et al.*<sup>19</sup> in the early 2000s, and the High Energy Resolution Fluorescence Detection (HERFD) spectra at the uranium  $M_4$ - and  $L_3$ -edges of  $Cs_2UO_2Cl_4$  was reported by Vitova *et al.*<sup>132</sup> in the past decade. In Figure 2, we compare the experimental data with our simulations.

As previously reported by Denning *et al.*<sup>19</sup>, the O K-edge absorption spectrum exhibits three prominent features (spectra **a** in Figure 2), identified as (**T1**) a low-intensity pre-edge feature at 531.4 eV corresponding to an  $O 1s \rightarrow \pi_u^*$  transition, followed by (**T2**) an intermediate-intensity pre-edge feature around 534.1 eV, arising from an  $O 1s \rightarrow \sigma_u^*$  transition, and (**T3**) the white-line feature at 536.5 eV, where an  $O 1s \rightarrow 2 \pi_g^*$  transition is observed.

Using the HERFD mode for the evaluation of the U  $M_4$ -edge spectra it is possible to achieve experimental spectral widths below the natural core-hole lifetime broadening of approximately 4 eV. As a result, the high-resolution U  $M_4$ -edge spectra in  $Cs_2UO_2Cl_4$  exhibit three well-defined features (spectra **b** in Figure 2), which have been reported in previous studies<sup>62,132</sup>: (**T4**) a  $U 3d_{5/2u} \rightarrow 5f \delta_u$  and  $U 3d_{5/2u} \rightarrow 5f \phi_u$  excitation observed at 3726.4 eV, (**T5**) a  $U 3d_{5/2u} \rightarrow 5f \pi_u^*$  resonance at 3728.6 eV, and a satellite peak (**T6**)  $U 3d_{5/2u} \rightarrow 5f \sigma_u^*$  at 3732.3 eV.

Interpreting the spectra at the U  $L_3$ -edge (marked as **c** in Figure 2) remains challenging due to the significant core-hole lifetime width spanned in this absorption edge, which extends between 7.4 – 8.4 eV<sup>11,59</sup>. This results in a significant portion of the spectral content being obscured. The first transition in this spectra is a  $2p_{3/2} \rightarrow 5f$  quadrupolar transition (**T7**) at 17168.8 eV, which could not be captured in our simulations, as they were performed within the electric dipole approximation. Besides that, the experimental white line is observed at 17175.2 eV, and our simulations predict that this feature it is mainly composed of (**T8**, **T9**) two  $2p_{3/2} \rightarrow 6d$  contributions, with a separation of 3.5 eV.

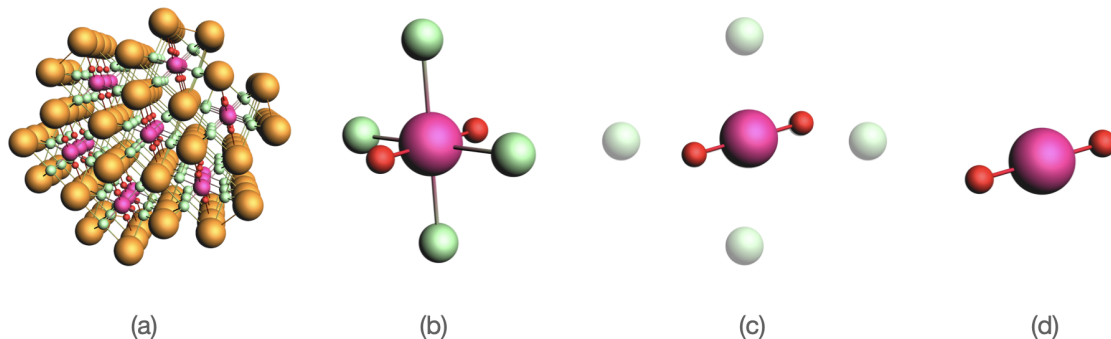


FIG. 1: Reference system for this study: (a) Dicesium uranyl(VI) tetrachloride crystal ( $\text{Cs}_2\text{UO}_2\text{Cl}_4$ ). Models here investigated: (b) uranyl(VI) tetrachloride dianion,  $\text{UO}_2\text{Cl}_4^{2-}$  (c) uranyl(VI) ion in the FDE embedding potential of four chloride atoms,  $\text{UO}_2^{2+} @ \text{Cl}_4^{4-}$  and (d) bare uranyl(VI) ion,  $\text{UO}_2^{2+}$  (cesium: orange; uranium: pink; oxygen: red; chlorine: green).

In Figure 2, the transition utilized to align the simulated spectra with their corresponding experimental data is depicted in orange and the energy shift values are displayed above each spectrum. The results of our simulations reveal that the energy shift values and differences between them become increasingly pronounced at higher absorption edges. For instance, at the O K-edge, the energy shift values for the 2- and 4-component simulations are respectively 13.3 eV and 13.8 eV, whereas, for the U  $L_3$ -edge, these values are 95.2 eV and 86.3 eV.

The increase of the shift for deeper cores is in line with the difficulty of TD-DFT to properly account for the orbital relaxation that should accompany the creation of a core hole, which will be increasingly important as the core orbitals under consideration become closer to the nucleus. This is already clearly illustrated for ionization energies, for which state-specific (e.g.  $\Delta\text{MP2}^{110}$  for small actinyls species) or coupled-cluster approaches (EOM-IP-CCSD<sup>39,111</sup> for heavy halogenated species), and more recently for excitation energies at the U  $M_4$ -edge of the bare uranyl using multiconfigurational approaches<sup>91,105,106</sup>. For instance, Polly *et al.*<sup>91</sup> evaluated the performance of various active spaces in SO-RASSCF and SO-RASPT2 simulations. Their results were found to overestimate experimental values by 12.9 eV and 17.4 eV at RASSCF and RASPT2 theory levels, respectively, which are about half of our results, which exhibited a discrepancy of 39.8 eV and 37.2 eV for 2- and 4-component calculations, respectively.

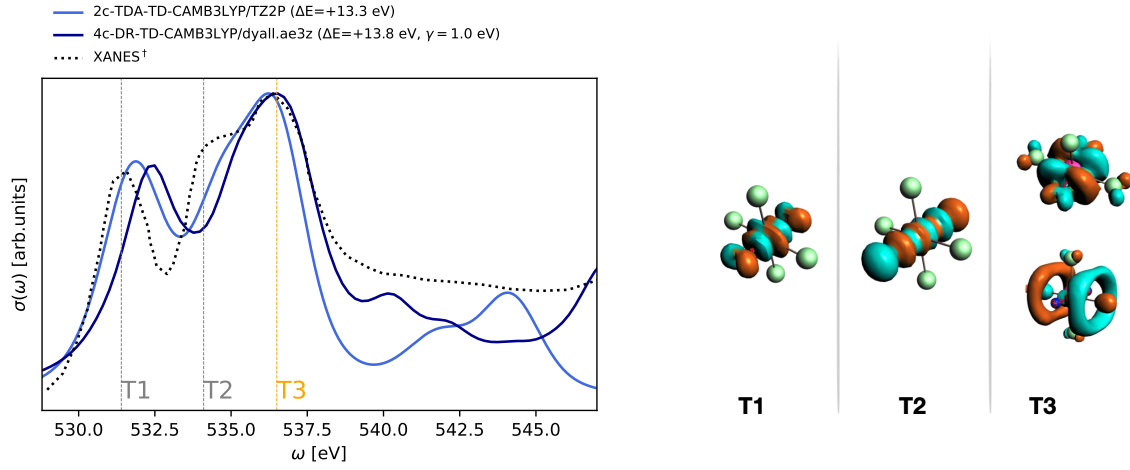
The relatively modest changes upon including dynamical electron correlation (about 5 eV) are consistent with the findings of South *et al.*<sup>110</sup> on the contribution from electron correlation (at MP2 level) to the binding energies in uranyl, as most of the core hole relaxation is coming from the orbital optimization enabled by the RASSCF approach. It is nevertheless interesting to note that the RASSCF calculations are closer to the experiment than RASPT2, suggesting a possible cancellation of errors when comparing the bare uranyl to the experimen-

tal system. We will return to this point when discussing the performance of embedding.

The damping factor employed for determining the DR-TD-DFT absorption spectra shown in Figure 2 were selected to best reflect the profile observed in the experimental data for the  $\text{Cs}_2\text{UO}_2\text{Cl}_4$  crystal, after exploring different values for each edge. For the oxygen K-edge, the value is somewhat larger ( $\gamma = 1.0$  eV) than for the uranium  $M_4$  and  $L_3$  edges ( $\gamma = 0.5$  eV), but nevertheless our results show that with these choices the key features of both conventional and high-resolution spectra can be clearly identified. We note that the value for the  $L_3$  edge was utilized for the purpose of comparison with the 2-component simulation. A more detailed comparison of the impact of a different damping factor on spectral profiles is presented in the supplementary information. There, we also provide a comparison of different line profile functions. The broadening profile presented in Figure 2 was a Voigt function for the O K-edge and U  $L_3$ -edge spectra, and a Gaussian function for the U  $M_4$ -edge simulation.

## 2. Polarization dependence of calculated intensities

Synchrotron-based experiments can also handle dichroism in the X-ray regime. Linear dichroism is studied using angle-resolved and polarization-dependent X-ray absorption spectra<sup>19,30,132</sup>, while magnetic circular dichroism has been extensively studied through X-ray magnetic circular dichroism (XMCD)<sup>63,80</sup>. By utilizing the damped-response theory, linear dichroism can be explored through the analysis of the components of the complex polarizability tensor ( $\alpha_{xx}(\omega)$ ,  $\alpha_{yy}(\omega)$ ,  $\alpha_{zz}(\omega)$ ). As we shall see in the following, the breakdown into individual components—or here, due to the symmetry of the system into parallel ( $\sigma_{zz}$ ) and perpendicular ( $\sigma_{xx+yy}$ ) components with respect to the uranyl bond axis—is use-



(a) O K-edge spectra.

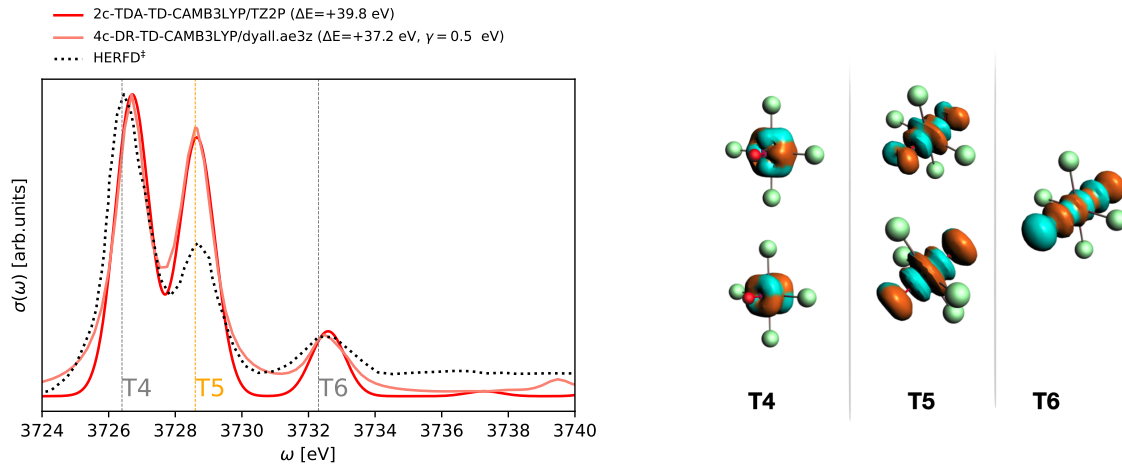
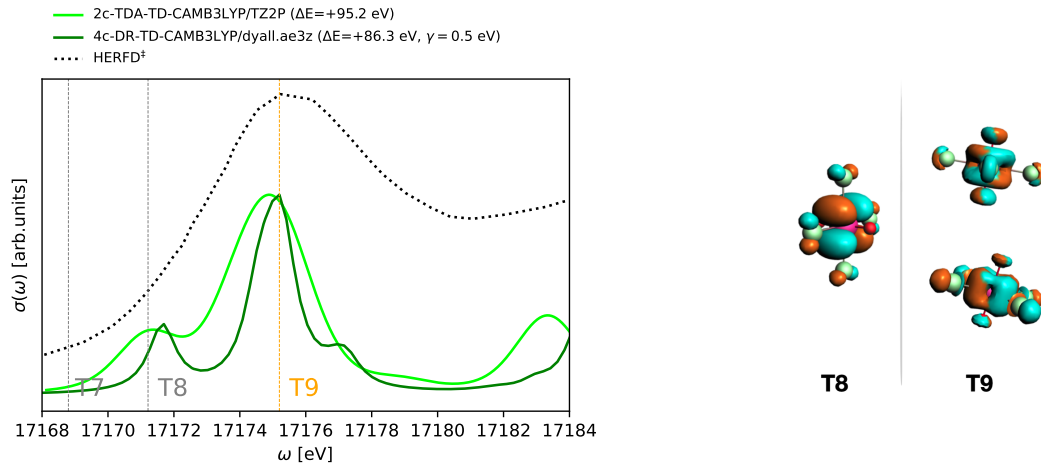
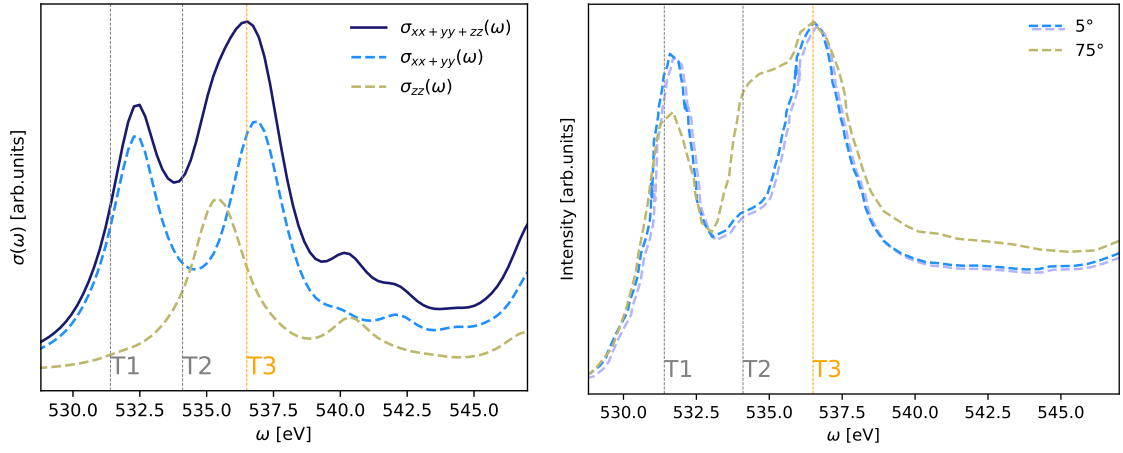
(b) U M<sub>4</sub>-edge spectra.(c) U L<sub>3</sub>-edge spectra.

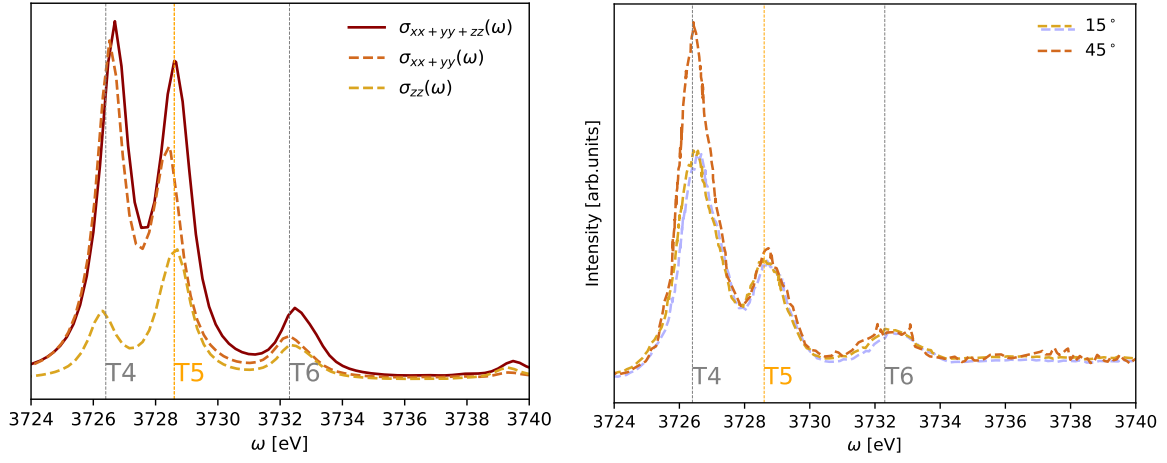
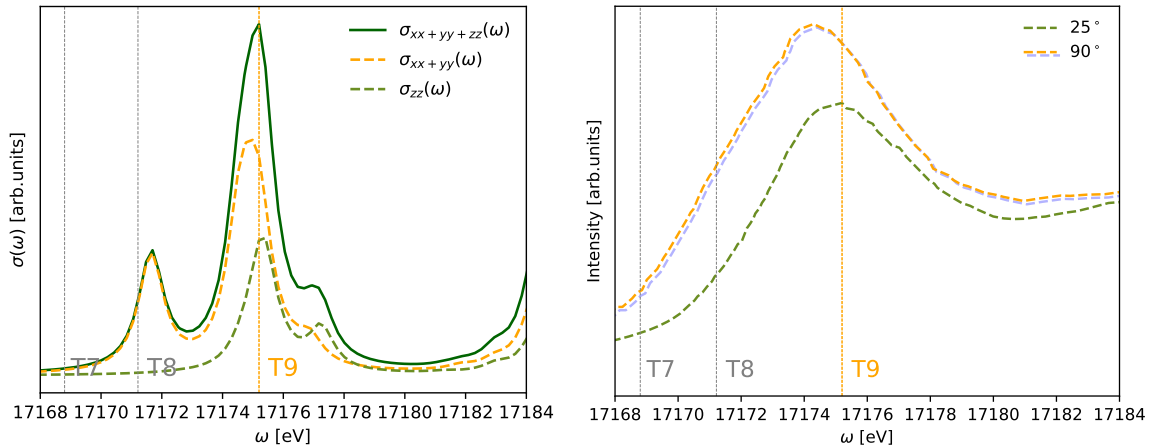
FIG. 2: Left: 4c-DR-TD-CAMB3LYP and 2c-TDA-TD-CAMB3LYP XAS spectra at the (a) O K-edge, (b) U M<sub>4</sub>- and (c) L<sub>3</sub>-edges of  $\text{UO}_2\text{Cl}_4^{2-}$ . Experimental data at the O K-edge and U M<sub>4</sub> and L<sub>3</sub>- edges of  $\text{Cs}_2\text{UO}_2\text{Cl}_4$  digitalized from references <sup>†19</sup> and <sup>†132</sup>, respectively. Right: Dominant NTOs from 2-component simulations. Isosurface value: 0.3. Labels and artificial broadening employed in the 2-component simulations are discussed in the text.



4c-DR-TD-CAMB3LYP simulation.

Angle-Resolved XANES<sup>19</sup>.

(a) O K-edge spectra.

(b) U M<sub>4</sub>-edge spectra.

4c-DR-TD-CAMB3LYP simulation.

Angle-Resolved HERFD<sup>132</sup>.(c) U L<sub>3</sub>-edge spectra.

FIG. 3: Left: Partial contributions to total oscillator strengths in the 4c-DR-TD-CAMB3LYP XAS spectra at (a) oxygen K-edge and uranium (b) M<sub>4</sub>- and (c) U L<sub>3</sub>-edges of  $\text{UO}_2\text{Cl}_4^{2-}$ . Right: Experimental data ( $\text{Cs}_2\text{UO}_2\text{Cl}_4$ ) at the O K-edge, U M<sub>4</sub> and U L<sub>3</sub>-edges digitized from<sup>19,132</sup>. The angle indicated in the figures corresponds to the angle between the incident light beam and the O-U-O axis., respectively.

ful to understand the origin of the asymmetries observed experimentally.

In Figure 3 we show the parallel and perpendicular contributions to the total absorption cross-section (Eq. 4) for the edges under investigation, alongside the experimental polarization-dependent spectra<sup>19,132</sup>, in which the angle indicated is the one between the incident light beam and the O-U-O axis in the  $\text{Cs}_2\text{UO}_2\text{Cl}_4$  crystal.

Effects of polarization dependence are particularly prominent in the experimental spectra at the O K-edge Denning *et al.*<sup>19</sup> and U  $L_3$ -edge Vitova *et al.*<sup>132</sup> (respectively **a** and **c** in Figure 3), which experimentally were recorded at greater incidence angles than the ones for U  $M_4$ . For clarity, here we will compare our results to the experiments under grazing and nearly perpendicular light incidence conditions.

For the O K-edge, our analysis finds that transitions **T1** and **T3** are dominated by be perpendicularly polarized components with respect to the O-U-O axis, whereas **T2** was found to exhibit parallel polarization, in agreement with experiment. For the  $L_3$ -edge, we observe that **T8** is completely dominated by perpendicularly polarized components. For **T9** shows non-negligible contributions from the parallel component, which we consider to be consistent with the observation by Vitova and co-workers<sup>132</sup> that angle dependence shifts the U  $L_3$ -edge absorption edge to the right when incoming light is parallel to the O-U-O axis.

Finally, for the U  $M_4$  edge (shown as **b** in Figure 3), a strong angular dependence in the white line (**T4**) is observed, and as for the other edges, the perpendicular components are the major contributors to the intensity. For **T5** we see that the parallel component contributes proportionally more to the total signal, and this trend is accentuated for **T6**, for which we see nearly equal contributions from both components to the total intensity.

### 3. Comparison of structural models

In this section, we compare the DR-TD-DFT spectral profiles discussed above for  $\text{UO}_2\text{Cl}_4^{2-}$  to those of two additional, simpler models at the same theoretical level, the bare uranyl ion and the uranyl ion embedded onto the equatorial chloride ligands. The embedded uranyl model was previously investigated for valence excited state<sup>35</sup> and shown to yield a rather good description of the low-lying states of  $\text{UO}_2\text{Cl}_4^{2-}$  in  $\text{Cs}_2\text{UO}_2\text{Cl}_4$ . Given the high sensitivity of core excited states to the description of the environment around the absorbing sites, it remains to be seen to which extent the embedded model can faithfully reproduce the reference ( $\text{UO}_2\text{Cl}_4^{2-}$ ) calculations.

At the O K-edge (marked as **a** in Figure 4), there are rather small differences between the energy shifts (less than 1 eV) with respect to experiment among the three simulations, which is in line with a systematic error in the calculations due to the shortcomings in describing relaxation due to the creation of the core hole. For the

intensities, on the other hand, we observe for **T1** that the bare uranyl model shows a significant overestimation. Intensities for the reference and embedded models on the other hand are very similar to one another, though the maximum for the embedded model is slightly shifted to lower energies. For **T2**, we observe that calculations with the embedding model exhibit shoulder as in the reference calculation, which is absent for the bare uranyl, even though this feature is somewhat less marked in calculations than in the experiment. Finally, the embedding calculation shows a broader structure around **T3**, presenting another maximum after the white line, which is more marked than in the reference model. We found that this feature disappears with a slightly larger damping factor.

The simulations at the U  $M_4$ -edge spectra (marked as **b** in Figure 4) show an even better agreement between the embedding calculations and the reference ones than for the O K edge, with both simulations reproducing experiment rather well for all peaks. However, if the splitting between **T4** and **T5** is very well reproduced, we see that for the embedding calculation **T6** there is a slight shift in peak maximum to higher energies compared both to experiment and to the reference model while the latter two show again very good agreement. For the bare uranyl, on the other hand, we see a fairly significant overestimation of both **T4-T5** and **T5-T6** peak shifts compared to the reference model.

Here it is interesting to recall that the solid-state community commonly attributes variations in peak splitting between the main feature and the satellite 5f  $\sigma^*$  in actinyl spectra to changes in overlap-driven covalency from variations in the An – O bond length, as suggested in the works of Kvashnina and Butorin<sup>62</sup>, and Vitova and collaborators<sup>132,134</sup>. This is somewhat at odds with the analysis based on *ab initio* simulations, such as those by Sergentu, Duignan, and Autschbach<sup>106</sup> and also Polly *et al.*<sup>91</sup>, which claim that there is not a clear correlation between those and the observed splitting in this spectrum. The natural localized molecular orbitals (NLMOs) analysis by Sergentu, Duignan, and Autschbach<sup>106</sup> found a significant decrease in the  $\sigma$  covalency in the excited states of the actinyl absorption spectra at the  $M_4$ -edge of  $\text{PuO}_2^{2+}$ ,  $\text{NpO}_2^{2+}$ , and  $\text{UO}_2^{2+}$ , in a trend that opposes the one observed in their ground states. Therefore, they were able to highlight the limitations of the previous interpretations of these spectra, by showing that the orbitals of the ground state should not be used as the sole guide in interpreting these actinyl spectra.

In Table I, we present the peak positions and splitting of the U  $M_4$ -edge spectra obtained from experiments by Vitova *et al.*<sup>132</sup> and predicted by *ab-initio* calculations (Sergentu, Duignan, and Autschbach<sup>106</sup>, Polly *et al.*<sup>91</sup> and this work). As previously discussed, the shortcomings of DR-TD-DFT calculations in including relaxation result in excitation energies that are too low compared to experiment or RASSCF/RASPT2.

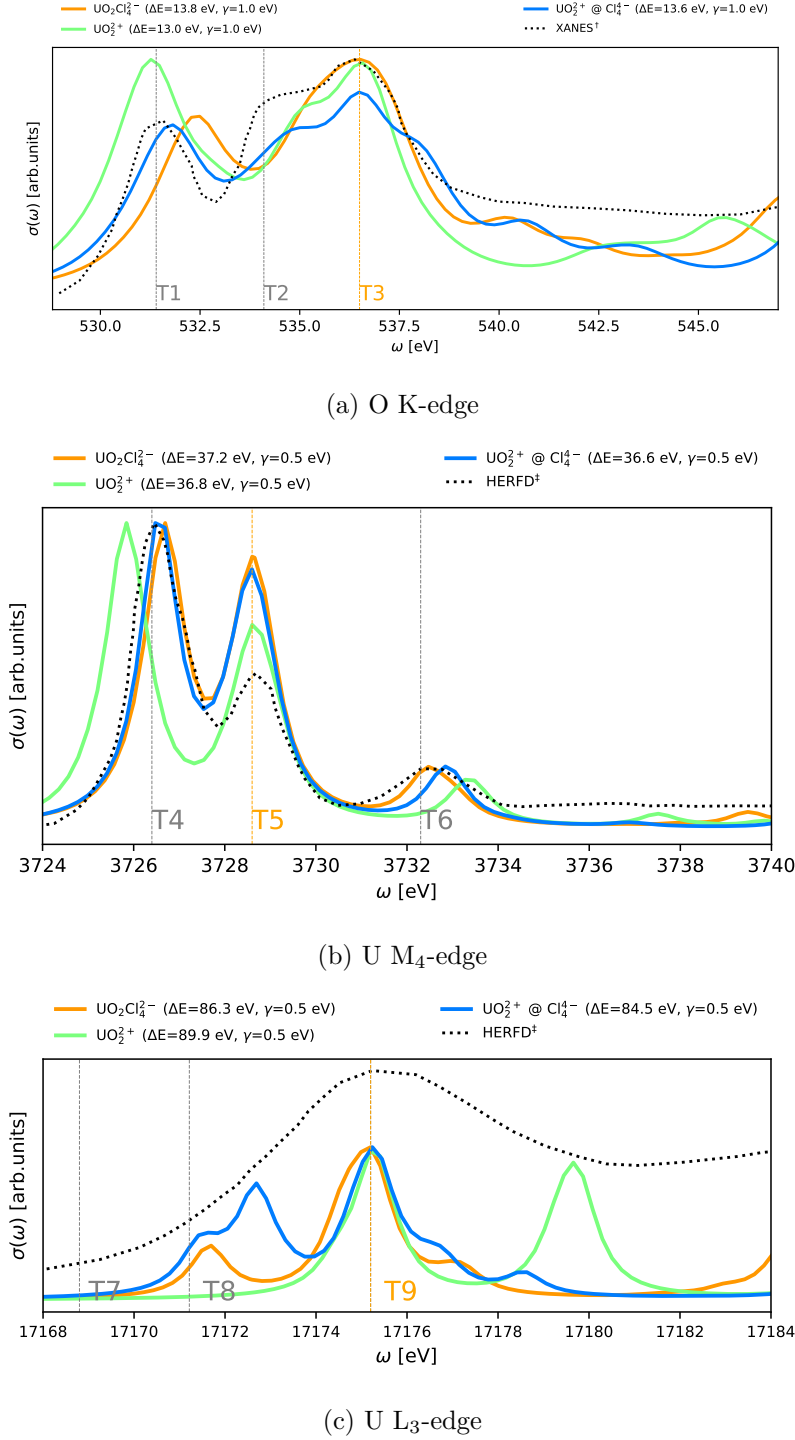


FIG. 4: Comparison of the 4c-DR-TD-CAMB3LYP XAS spectra at the oxygen K-edge, uranium  $M_4$  and  $L_3$ -edges of  $\text{UO}_2^{2+}$ ,  $\text{UO}_2^{2+} @ \text{Cl}_4^{4-}$  and  $\text{UO}_2\text{Cl}_4^{2-}$ . Experimental data at the O K-edge and U  $M_4$  and  $L_3$ - edges of  $\text{Cs}_2\text{UO}_2\text{Cl}_4$  digitalized from references  $\dagger^{19}$  and  $\dagger^{132}$ , respectively.

The peak splitting values, on the other hand, indicate that in spite of better accounting for orbital relaxation, RASSCF and RASPT2 calculations do not compare more favorably to experiment than DR-TD-DFT, and changing the size of the active space changes peak positions

by a few eV but peak splittings by a few tenths of eV. Taken as a whole we attribute the overestimation of peak splittings for all of these calculations to the lack of equatorial ligands, since when these are included (embedding or supermolecular DR-TD-DFT calculations) we

TABLE I: U M<sub>4</sub>-edge peak positions and differences (in eV) from theoretical (DR-TD-DFT, RASPT2 and RASSCF) and experiment (HERFD).

Method	System	peak positions			differences		
		<b>T4</b>	<b>T5</b>	<b>T6</b>	<b>T5-T4</b>	<b>T6-T4</b>	<b>T6-T5</b>
DR-TD-DFT	UO <sub>2</sub> <sup>2+</sup>	3689.0	3691.8	3696.5	2.8	7.5	4.7
RASSCF <sup>106</sup>	UO <sub>2</sub> <sup>2+</sup>	3750.1	3752.4	3758.0	2.3	7.9	5.6
RASSCF <sup>a91</sup>	UO <sub>2</sub> <sup>2+</sup>	3748.0	3750.1	3755.7	2.1	7.7	5.6
RASSCF <sup>b91</sup>	UO <sub>2</sub> <sup>2+</sup>	3750.6	3753.1	3759.4	2.5	8.8	6.3
RASPT2 <sup>b91</sup>	UO <sub>2</sub> <sup>2+</sup>	3746.1	3748.8	3755.1	2.7	9.0	6.3
DR-TD-DFT	UO <sub>2</sub> <sup>2+</sup> @ Cl <sub>4</sub> <sup>4-</sup>	3690.1	3692.0	3696.2	1.9	6.1	4.2
DR-TD-DFT	UO <sub>2</sub> Cl <sub>4</sub> <sup>2-</sup>	3689.5	3691.4	3695.3	1.9	5.8	3.9
HERFD <sup>132</sup>	Cs <sub>2</sub> UO <sub>2</sub> Cl <sub>4</sub>	3726.4	3728.6	3732.3	2.2	5.9	3.7

Active space: <sup>a</sup> 3d ( $\sigma_u, \pi_u$ )/5f, <sup>b</sup> 3d/5f

achieve very good agreement with the experiment, especially for the **T6-T4** and **T6-T5** splittings. It is interesting to note that the RASPT2 approach, which one could expect to improve upon RASSCF, ends up further overestimating peak splittings. This could be due to a poor balance between orbital relaxation and the amount of dynamic correlation recovered with second-order perturbation theory, possibly coupled to the lack of equatorial ligands in the calculations.

Coming back to the **T6-T4** and **T6-T5** splittings, we observe slight differences between the embedding and supermolecule calculations, which point to orbital interactions being somewhat more important for **T6** than for **T4** or **T5**—since in the embedding calculation, the chloride ligands are only included via the embedding potential and therefore represent an effective interaction, there are by construction no explicit effects such as hybridization between the uranyl subunit and the equatorial ligands. While the embedding potential does account for non-classical contributions from electron correlation and exchange between subsystems, the electrostatic interaction component of the embedding potential remains a dominant contribution. Given the similarity of our embedding results and the supermolecular calculation suggests that covalency between uranium and equatorial ligands not to be a very important parameter for understanding the system’s ground or excited states, or at least not as important as argued by Vitova *et al.*<sup>132</sup>.

At the U L<sub>3</sub>-edge (depicted as **c** in Figure 4) we have obtained the same results as South *et al.*<sup>110</sup> for the uranyl ion, which presents a second feature that is not present in any spectra recorded for uranium-containing species. The embedding calculation presents a broader and more intense **T8** feature, with the **T9** resembling rather well that of the reference model, with the following feature being more intense to the anion case and being shifted to the right.

Finally, in the following, we will not consider more sophisticated models in which the crystal environment in Cs<sub>2</sub>UO<sub>2</sub>Cl<sub>4</sub> beyond the equatorial chloride ligands (struc-

ture **a** in Figure 1) are included in the embedding potential since in our previous investigation of valence excited states<sup>35</sup>, we have determined that the additional environment did not significantly alter the values of different (valence) excitation energies, but rather introduces a nearly constant shift of orbital energies.

## B. Photoionization

In this section, we present our results for core binding energies for the oxygen K edge and different uranium edges. One of our goals is to assess the performance of embedding as done above for DR-TD-DFT. The other, given the scarcity of experimental data for the uranyl tetrachloride species, is to investigate how different parameters (Hamiltonian, etc.) impact the absolute binding energies, thus complementing the investigation carried out by Halbert *et al.*<sup>39</sup> but now focusing on a heavier center. Due to constraints in computational resources, we shall employ double-zeta basis sets in most calculations.

Starting with the effect of the Hamiltonian – which due to constraints on the computational resources we have only evaluated for the highly symmetrical UO<sub>2</sub><sup>2+</sup> species – we observe from the results in Table II that the differences in binding energies between reference <sup>4</sup>DC and the <sup>2</sup>DC<sup>M</sup> calculations – which are computationally less expensive, notable in the transformation to molecular spinor basis – are generally very small ( $\simeq 0.3$  eV or less, in absolute value) and can therefore be considered negligible apart from the uranium K edge ( $\simeq 2.4$  eV, in absolute value).

As discussed by Halbert *et al.*<sup>39</sup>, this difference is due to the two-electron picture change error that is introduced in the transformation to a two-component Hamiltonian for <sup>2</sup>DC<sup>M</sup>. This difference follows on the trend observed for the halides<sup>39</sup>, that is, it increases with increased atomic number, but only modestly so in comparison to astatide ( $\simeq 1.7$  eV, in absolute). This means that one should not expect it to become a significant source

of error in calculations for actinides and beyond (super-heavy elements), especially given the very high energy of the K edges for such systems—for comparison, the error for the K edge corresponds to 0.0021% of the calculated binding energy.

As can be seen in Table II, for the uranium atom a more important parameter than corrections to picture change effects is the explicit inclusion of (SS|SS)-type integrals. These tend to decrease the K, L, and M edges and increase the N edge binding energies. Compared to the values for astatide, the decrease for the K, L, and M edges is nearly twice as large, whereas for the N edges values are nearly equivalent to those for astatide. As previously found, effects for the edges involving the  $p_{1/2}$  spinors are larger than for the other spinors for a given shell.

The current-current contributions to the two-electron interactions, partially included via the Gaunt interactions, are much more significant, and can be up to nearly an order of magnitude larger than the (SS|SS)-type integrals (e.g. 525 eV for Gaunt vs 70 eV for (SS|SS) in the case of the K edge, 68 eV for Gaunt vs 6 eV for (SS|SS) in the case of the  $L_3$  edge, etc).

Besides these two main effects, the remaining part of the current-current two-electron interaction (the gauge term) and QED effects are also significant, but at this time they cannot be explicitly taken into account in calculations with DIRAC. For that, we proceeded as done elsewhere in the literature<sup>39,111</sup> and employed atomic corrections based on the work of Koziol and Aucar<sup>58</sup>. In table S4 we present our CVS-EOM-IP-CCSD results for the bare uranyl ion including QED+Breit corrections.

## 1. Effects of the environment

Table III displays the ionization energy values obtained from CVS-EOM-IP calculations for the three models studied using double- and triple-zeta basis sets. Due to the constraints of employing uncontracted basis sets, and of limitations on the computational resources at our disposal, for the supermolecule we were only capable of carrying out calculations double-zeta bases, and restricting the virtual space to spinors with energies up to about 200  $E_h$ , meaning that in striving for an unbiased comparison, we had to enforce a similar constraint to the bare and embedded uranyl models.

For heavy halides, we had found that in order to achieve high accuracy for deeper edges<sup>39</sup> it was necessary to correlate high-lying virtuals—meaning that, for example, for the K edge we had to correlate all electrons and all virtuals. Thus, we carried out an investigation of the effect of the virtual spinor cutoff on the binding energies of the uranium K, L, M, and N edge on the bare uranyl system, for which the calculations were carried out in  $D_{\infty h}$  symmetry.

From our results, which can be found in tables II and III of the supplementary material, we observe very

large variations (about 39 eV) for the K edge binding energies as we go from the full virtual space to a truncation to keep roughly 60% of the virtual space. For the L edge, we also observe non-negligible variations (up to 10 eV for the  $L_3$  edge), but for the M and N edges, such virtual space truncations do not bring about significant errors (around 1 eV or less) compared to the full virtual space. With that, we concluded that we could safely investigate the M and N edges even when limiting our correlating (occupied and virtual) space to spinors with energies between -200 and 200  $E_h$ . For the bare uranyl ion, using this energy interval implies only including 61.4% of the virtual orbitals available with a double-zeta basis.

Going back to a comparison of models, we observe that when going from the bare to the embedded uranyl, the binding energies show fairly important changes, ranging from around -10 eV for the  $M_4$  edge and up to about -21 eV for N edges. It is interesting to note that for the oxygen K edge, which is in a similar energy range as part of the N edges, there is also a significant change (around -21 eV) to binding energies, underscoring that taking into account the effect of the equatorial ligands is as important to the center to which they are directly bound (uranium) as well as to those further away.

Comparing the embedded uranyl to the supermolecular system, we also see some differences, but they are more systematic and range from -2.6 eV for the M edges, to between -2 to -3 eV for the N edges, and fall to about -1 eV for the oxygen K edge. As was observed for the DR-TD-DFT calculations, these results give additional support to our claim that the embedded uranyl is actually a very cost-effective model for the uranyl tetrachloride system.

For the bare and embedded uranyl, we were able to carry out triple-zeta calculations, with the same correlation space as for the double-zeta bases. While we find the same overall trends, we now see a more systematic difference between the bare and embedded uranyl, with differences of around -19 to -20 eV for all edges considered. The difference between the double- and triple-zeta results resides in an increase in binding energies of about 10 eV for the bare uranyl M edge, while the binding energies for embedded uranyl varied very little (not more than 0.2 eV).

While we are not aware of experimental results for these binding energies, we nevertheless provide on Table III a theoretical estimate for the uranium M and N edges, and oxygen K edge, of uranyl tetrachloride in  $\text{Cs}_2\text{UO}_2\text{Cl}_4$ , via a combination of embedded uranyl results, atomic corrections for Breit and QED effects, and energy shifts to account for (a) the orbital interactions between the chlorides and the uranyl (from the difference between embedded uranyl and uranyl tetrachloride for double zeta basis sets, from our current results) and (b) the effect of the crystal environment on binding energies<sup>35</sup>, taken to be a constant shift of about 5 eV on all energies. We note that this value does not account for the relaxation of the electronic structure of the crystal

TABLE II: Differences in core electron binding energies with respect to reference  $^4\text{DC}$  values ( $\Delta E$ , in eV), for uranium and oxygen in  $\text{UO}_2^{2+}$ . Uncontracted Dyall double-zeta basis sets<sup>24,25</sup> are used for all atoms. We note that lines with different values for a given edge correspond to splitting due to the lowering of symmetry in the molecular system compared to the isolated atoms.

Atom	edge	$^4\text{DC}$ (SS SS)	$^2\text{DC}^M$	$^2\text{DC}^M$ (SS SS)	$^2\text{DCG}^M$	$^2\text{DCG}^M$ (SS SS)
U	K	-68.44	-2.42	-69.57	-525.14	-591.68
	L <sub>1</sub>	-12.56	-0.14	-12.58	-64.17	-76.72
	L <sub>2</sub>	-17.97	0.02	-17.83	-107.87	-125.57
	L <sub>3</sub>	-5.86	-0.28	-6.08	-68.52	-74.27
		-5.85	-0.28	-6.07	-68.51	-74.26
	M <sub>1</sub>	-3.16	$< 3 \times 10^{-3}$	-3.14	-12.68	-15.80
	M <sub>2</sub>	-4.10	0.02	-4.08	-21.44	-25.51
	M <sub>3</sub>	-1.52	-0.02	-1.54	-13.13	-14.64
		-1.53	-0.03	-1.55	-13.13	-14.64
	M <sub>4</sub>	-1.43	0.02	-1.40	-9.52	-10.92
		-1.42	0.02	-1.39	-9.50	-10.90
	M <sub>5</sub>	-0.21	-0.05	-0.26	-6.71	-6.92
		-0.22	-0.06	-0.27	-6.70	-6.92
		-0.22	-0.06	-0.27	-6.70	-6.91
	N <sub>1</sub>	-0.83	0.01	-0.82	-2.93	-3.76
	N <sub>2</sub>	-1.03	0.01	-1.03	-5.03	-6.06
	N <sub>3</sub>	-0.37	$< 2 \times 10^{-3}$	-0.37	-2.79	-3.16
		-0.37	$< 1 \times 10^{-4}$	-0.37	-2.78	-3.15
	N <sub>4</sub>	-0.30	$< 2 \times 10^{-3}$	-0.29	-1.59	-1.89
		-0.29	0.01	-0.29	-1.58	-1.87
	N <sub>5</sub>	-0.02	-0.01	-0.02	-0.92	-0.93
		-0.01	$< 2 \times 10^{-3}$	-0.01	-0.91	-0.92
		-0.01	$< 3 \times 10^{-3}$	-0.01	-0.90	-0.92
	N <sub>6</sub>	0.05	0.01	0.05	0.06	0.10
		0.04	$< 6 \times 10^{-4}$	0.05	0.06	0.10
	N <sub>7</sub>	0.05	0.01	0.05	0.07	0.12
		0.16	-0.01	0.15	0.36	0.52
		0.16	-0.01	0.15	0.36	0.52
		0.16	$< 3 \times 10^{-3}$	0.16	0.37	0.53
		0.17	$< 2 \times 10^{-3}$	0.16	0.37	0.53
O	K	0.00	0.00	0.00	-0.11	-0.11
		0.00	0.00	0.00	-0.11	-0.11

environment upon the creation of the core hole—for valence ionizations, this relaxation was estimated to be of around 1 eV.

## V. CONCLUSIONS

We have carried out an evaluation of relativistic quantum chemistry approaches for the calculation of excitation and ionization energies at the oxygen K-edge and uranium M<sub>4</sub>-, L<sub>3</sub>-edges for the uranyl ion in the gas phase and as a host in the Cs<sub>2</sub>UO<sub>2</sub>Cl<sub>4</sub> crystal by including its four chloride equatorial ligands by means of a frozen density embedding potential. Additionally, we have also assessed the UO<sub>2</sub>Cl<sub>4</sub><sup>2-</sup> system. We utilized standard and damped response theory to assess excitation energies and employed equation of motion coupled cluster simulations to determine absolute binding energies.

With respect to excitation energies, the use of the Coulomb-attenuating functional CAM-B3LYP in re-

sponse simulations produced results that are consistent with the features observed in both conventional XANES and HERFD experiments. Additionally, our two-component simulations and analysis of the natural transition orbitals (NTOs) showed that the O K-edge spectra primarily provide insight into the low-lying anti-bonding states centered in the uranyl unit ( $\pi_u^*$ ,  $\sigma_u^*$  and  $\pi_g^*$ ). In contrast, the lowest energy orbitals accessed at the U M<sub>4</sub>- ( $\phi_u$ ,  $\delta_u$ ) and U L<sub>3</sub>- ( $\delta_g$ ) absorption edges are the uranium 5*f* and 6*d* non-bonding orbitals. These observations are in line with previous investigations.

In the soft and tender x-ray regime (O K- and U M<sub>4</sub>-edge, respectively), we have observed that our simulations in the gas phase and for the embedded model yield both excitation energies and intensities near to those obtained for the UO<sub>2</sub>Cl<sub>4</sub><sup>2-</sup> ion. However, when considering the hard x-rays regime (U L<sub>3</sub>-edge), it was observed that the smaller models deviated more significantly from the results obtained from the anion.

This investigation was complemented by CVS-IP-

TABLE III: CVS-EOM-CCSD core ionization potentials (in eV) for  $\text{UO}_2^{2+}$ ,  $\text{UO}_2^{2+} @ \text{Cl}_4^{4-}$  and  $\text{UO}_2\text{Cl}_4^{2-}$  using double- and triple-zeta basis set for all atoms. All calculations were performed with the <sup>4</sup>DC Hamiltonian. Here estimate denotes corrections to the  $\text{UO}_2^{2+} @ \text{Cl}_4^{4-}$  triple-zeta results including corrections for QED, Breit and crystal environment effects .

Atom	Edge	double zeta			triple zeta		estimate
		$\text{UO}_2^{2+}$	$\text{UO}_2^{2+} @ \text{Cl}_4^{4-}$	$\text{UO}_2\text{Cl}_4^{2-}$	$\text{UO}_2^{2+}$	$\text{UO}_2^{2+} @ \text{Cl}_4^{4-}$	$\text{Cs}_2\text{UO}_2\text{Cl}_4$
U	M <sub>4</sub>	3755.78	3745.42	3742.79	3765.11	3737.21	3742.21
		3756.06	3745.19	3742.61	3765.37	3736.99	3741.99
	M <sub>5</sub>	3577.91	3564.93	3562.28	3584.47	3559.43	3564.43
		3578.05	3564.67	3562.07	3584.60	3559.17	3564.17
		3578.36	3564.55	3561.97	3584.90	3559.05	3564.05
	N <sub>1</sub>	1477.83	1460.61	1457.72	1480.64	1455.13	1460.13
	N <sub>2</sub>	1308.09	1292.95	1290.09	1313.00	1287.87	1292.87
	N <sub>3</sub>	1075.35	1058.92	1055.23	1078.01	1056.08	1061.08
		1076.39	1058.02	1055.91	1079.02	1055.18	1060.18
	N <sub>4</sub>	809.65	791.91	788.31	811.08	790.41	795.41
		810.59	791.10	788.92	811.99	789.60	794.60
	N <sub>5</sub>	766.46	748.35	744.48	767.21	747.51	752.51
		766.94	747.67	744.81	767.68	746.83	751.83
		767.73	747.25	745.30	768.44	746.41	751.41
		416.12	396.85	393.34	415.95	396.74	401.74
	N <sub>6</sub>	416.47	396.21	393.13	416.29	396.11	401.11
		417.20	395.91	393.82	417.00	395.81	400.81
	N <sub>7</sub>	405.10	385.77	381.96	404.63	385.66	390.66
		405.30	385.23	381.84	404.83	385.13	390.13
		405.80	384.78	382.31	405.32	384.68	389.68
		406.44	384.61	382.68	405.94	384.51	389.51
O	K	555.37	534.29	533.00	555.41	534.24	539.24
		555.37	534.29	533.00	555.41	534.24	539.24

EOM-CCSD calculations, where we reported for the first time in the literature a study on core-level binding energies of heavy elements using such a high-level theory level. In this study, the significance of current-current interaction and the role of small-type integrals in evaluating hard x-ray binding energies were revealed. Additionally, the application of the FDE approach demonstrated that the electrostatic field of the chloride ligand has a significant impact on shifting energy levels in the uranyl unit even at the soft x-ray regime, as shown for the oxygen 1s binding energy.

These findings highlight the limitations of relying solely on a bare uranyl approximation when studying actinide core spectroscopy at higher energies and the potential of using uncoupled embedded models to simulate actinide core spectra semi-quantitatively.

## VI. ACKNOWLEDGMENTS

We acknowledge discussions with Dr. Valérie Vallet on carrying out the analysis of natural transition orbitals and on the manuscript. We acknowledge support from the Franco-German project CompRIXS (Agence nationale de la recherche ANR-19-CE29-0019, Deutsche Forschungsgemeinschaft JA 2329/6-1), PIA ANR project CaPPA (ANR-11-LABX-0005-01), I-SITE ULNE projects OVERSEE and MESONM International

Associated Laboratory (LAI) (ANR-16-IDEX-0004), the French Ministry of Higher Education and Research, region Hauts de France council and European Regional Development Fund (ERDF) project CPER CLIMIBIO, and the French national supercomputing facilities (grants DARI A0090801859, A0110801859, A0130801859).

<sup>1</sup>DIRAC, a relativistic ab initio electronic structure program, Release DIRAC22 (2022), written by H. J. Aa. Jensen, R. Bast, A. S. P. Gomes, T. Saue and L. Visscher, with contributions from I. A. Aucar, V. Bakken, C. Chibueze, J. Creutzberg, K. G. Dyall, S. Dubillard, U. Ekström, E. Eliav, T. Enevoldsen, E. Faßhauer, T. Fleig, O. Fossgaard, L. Halbert, E. D. Hedegård, T. Helgaker, B. Helmich-Paris, J. Henriksson, M. van Horn, M. Iliaš, Ch. R. Jacob, S. Knecht, S. Komorovský, O. Kulie, J. K. Lærdahl, C. V. Larsen, Y. S. Lee, N. H. List, H. S. Nataraj, M. K. Nayak, P. Norman, G. Olejniczak, J. Olsen, J. M. H. Olsen, A. Papadopoulos, Y. C. Park, J. K. Pedersen, M. Pernpointner, J. V. Pototschnig, R. di Remigio, M. Repisky, K. Ruud, P. Salek, B. Schimmelpfennig, B. Senjean, A. Shee, J. Sikkema, A. Sunaga, A. J. Thorvaldsen, J. Thyssen, J. van Stralen, M. L. Vidal, S. Villaume, O. Visser, T. Winther, S. Yamamoto and X. Yuan (available at <http://dx.doi.org/10.5281/zenodo.6010450>, see also <http://www.diracprogram.org>).

<sup>2</sup>Abney, C. W., Mayes, R. T., Saito, T., and Dai, S., “Materials for the recovery of uranium from seawater,” Chemical reviews **117**, 13935–14013 (2017).

<sup>3</sup>Barker, T. J., Denning, R. G., and Thorne, J. R., “Applications of two-photon spectroscopy to inorganic compounds. 2. spectrum and electronic structure of cesium uranyl nitrate, csuo<sub>2</sub>(no<sub>3</sub>)<sub>3</sub>,” Inorganic Chemistry **31**, 1344–1353 (1992).

- <sup>4</sup>Besley, N. A., "Density functional theory based methods for the calculation of x-ray spectroscopy," *Accounts of Chemical Research* **53**, 1306–1315 (2020).
- <sup>5</sup>Besley, N. A., "Modeling of the spectroscopy of core electrons with density functional theory," *Wiley Interdisciplinary Reviews: Computational Molecular Science* **11**, e1527 (2021).
- <sup>6</sup>Bonato, L., Viot, M., Dumas, T., Mesbah, A., Dalodière, E., Blanco, O. D., Wiss, T., Le Goff, X., Odorico, M., Prieur, D., *et al.*, "Probing the local structure of nanoscale actinide oxides: a comparison between puo 2 and tho 2 nanoparticles rules out puo 2+ x hypothesis," *Nanoscale Advances* **2**, 214–224 (2020).
- <sup>7</sup>Bouchafra, Y., Shee, A., Réal, F., Vallet, V., and Gomes, A. S. P., "Predictive simulations of ionization energies of solvated halide ions with relativistic embedded equation of motion coupled cluster theory," *Physical Review Letters* **121** (2018), 10.1103/physrevlett.121.266001.
- <sup>8</sup>Burke, K., Perdew, J. P., and Wang, Y., "Derivation of a generalized gradient approximation: The pw91 density functional," *Electronic Density Functional Theory: recent progress and new directions*, 81–111 (1998).
- <sup>9</sup>Butorin, S. M., Bauters, S., Amidani, L., Beck, A., Weiss, S., Vitova, T., and Tougait, O., "X-ray spectroscopic study of chemical state in uranium carbides," *Journal of Synchrotron Radiation* **29** (2022).
- <sup>10</sup>Caciuffo, R. and Lander, G. H., "X-ray synchrotron radiation studies of actinide materials," *Journal of Synchrotron Radiation* **28**, 1692–1708 (2021).
- <sup>11</sup>Campbell, J. and Papp, T., "Widths of the atomic k-n7 levels," *Atomic Data and Nuclear Data Tables* **77**, 1–56 (2001).
- <sup>12</sup>Christiansen, O., Jørgensen, P., and Hättig, C., "Response functions from fourier component variational perturbation theory applied to a time-averaged quasienergy," *International Journal of Quantum Chemistry* **68**, 1–52 (1998).
- <sup>13</sup>Coriani, S. and Koch, H., "Communication: X-ray absorption spectra and core-ionization potentials within a core-valence separated coupled cluster framework," *The Journal of Chemical Physics* **143**, 181103 (2015).
- <sup>14</sup>Crossland, L., *Nuclear fuel cycle science and engineering* (Elsevier, 2012).
- <sup>15</sup>De Jesus, K., Rodriguez, R., Baek, D., Fox, R., Pashikanti, S., and Sharma, K., "Extraction of lanthanides and actinides present in spent nuclear fuel and in electronic waste," *Journal of Molecular Liquids* **336**, 116006 (2021).
- <sup>16</sup>De Santis, M., Sorbelli, D., Vallet, V., Gomes, A. S. P., Storch, L., and Belpassi, L., "Frozen-density embedding for including environmental effects in the dirac-kohn-sham theory: An implementation based on density fitting and prototyping techniques," *Journal of Chemical Theory and Computation* (2022).
- <sup>17</sup>Denecke, M. A., Bryan, N., Kalmykov, S., Morris, K., and Quinto, F., "Sources and behaviour of actinide elements in the environment," in *Experimental and theoretical approaches to actinide chemistry* (Wiley Online Books, 2018).
- <sup>18</sup>Dennett, C. A., Poudel, N., Simmonds, P. J., Tiwari, A., Hurley, D. H., and Gofryk, K., "Towards actinide heterostructure synthesis and science," *Nature Communications* **13**, 2221 (2022).
- <sup>19</sup>Denning, R., Green, J., Hutchings, T., Dallera, C., Tagliaferri, A., Giarda, K., Brookes, N., and Braicovich, L., "Covalency in the uranyl ion: A polarized x-ray spectroscopic study," *The Journal of Chemical Physics* **117**, 8008–8020 (2002).
- <sup>20</sup>Denning, R., Snellgrove, T., and Woodward, D., "The electronic structure of the uranyl ion: Part i. the electronic spectrum of cs2uo2cl4," *Molecular Physics* **32**, 419–442 (1976).
- <sup>21</sup>Denning, R. G., "Electronic structure and bonding in actinyl ions and their analogs," *The Journal of Physical Chemistry A* **111**, 4125–4143 (2007).
- <sup>22</sup>Di Remigio, R., Bast, R., Frediani, L., and Saue, T., "Four-component relativistic calculations in solution with the polarizable continuum model of solvation: theory, implementation, and application to the group 16 dihydrides h2x (x= o, s, se, te, po)," *The Journal of Physical Chemistry A* **119**, 5061–5077 (2014).
- <sup>23</sup>Dyall, K. G., "Interfacing relativistic and nonrelativistic methods. i. normalized elimination of the small component in the modified dirac equation," *The Journal of chemical physics* **106**, 9618–9626 (1997).
- <sup>24</sup>Dyall, K. G., "Relativistic and nonrelativistic finite nucleus optimized triple-zeta basis sets for the 4 p, 5 p and 6 p elements," *Theoretical Chemistry Accounts* **108**, 335–340 (2002).
- <sup>25</sup>Dyall, K. G., "Relativistic double-zeta, triple-zeta, and quadruple-zeta basis sets for the light elements h–ar," *Theoretical Chemistry Accounts* **135**, 128 (2016).
- <sup>26</sup>Dyall, K. G. and Fægri Jr, K., *Introduction to relativistic quantum chemistry* (Oxford University Press, 2007).
- <sup>27</sup>Ernzerhof, M. and Scuseria, G. E., "Assessment of the perdue–burke–ernzerhof exchange–correlation functional," *The Journal of chemical physics* **110**, 5029–5036 (1999).
- <sup>28</sup>Ferenc, D., Korobov, V. I., and Mátyus, E., "Nonadiabatic, relativistic, and leading-order qed corrections for rovibrational intervals of he 4 2+(x  $\sigma$  2 u+)," *Physical Review Letters* **125**, 213001 (2020).
- <sup>29</sup>Fransson, T., Coriani, S., Christiansen, O., and Norman, P., "Carbon x-ray absorption spectra of fluoroethenes and acetone: A study at the coupled cluster, density functional, and static-exchange levels of theory," *The Journal of Chemical Physics* **138**, 124311 (2013).
- <sup>30</sup>Frati, F., Hunault, M. O., and De Groot, F. M., "Oxygen k-edge x-ray absorption spectra," *Chemical reviews* **120**, 4056–4110 (2020).
- <sup>31</sup>Ganguly, G., Sergentu, D.-C., and Autschbach, J., "Ab initio analysis of metal–ligand bonding in an (cot) 2 with an= th, u in their ground- and core-excited states," *Chemistry–A European Journal* **26**, 1776–1788 (2020).
- <sup>32</sup>Gibson, J. K. and de Jong, W. A., "Experimental and theoretical approaches to actinide chemistry," (2018).
- <sup>33</sup>Golubev, N. V., Vaníček, J., and Kuleff, A. I., "Core-valence attosecond transient absorption spectroscopy of polyatomic molecules," *Physical Review Letters* **127**, 123001 (2021).
- <sup>34</sup>Gomes, A. S. P. and Jacob, C. R., "Quantum-chemical embedding methods for treating local electronic excitations in complex chemical systems," *Annual Reports Section "C" (Physical Chemistry)* **108**, 222–277 (2012).
- <sup>35</sup>Gomes, A. S. P., Jacob, C. R., Réal, F., Visscher, L., and Vallet, V., "Towards systematically improvable models for actinides in condensed phase: the electronic spectrum of uranyl in cs 2 uo 2 cl 4 as a test case," *Physical Chemistry Chemical Physics* **15**, 15153–15162 (2013).
- <sup>36</sup>Gomes, A. S. P., Jacob, C. R., and Visscher, L., "Calculation of local excitations in large systems by embedding wave-function theory in density-functional theory," *Physical Chemistry Chemical Physics* **10**, 5353 (2008).
- <sup>37</sup>Grambow, B., Nitta, A., Shibata, A., Koma, Y., Utsunomiya, S., Takami, R., Fueda, K., Ohnuki, T., Jegou, C., Laffolley, H., *et al.*, "Ten years after the npp accident at fukushima: review on fuel debris behavior in contact with water," *Journal of Nuclear Science and Technology* **59**, 1–24 (2022).
- <sup>38</sup>Gulania, S., Kjørstad, E. F., Stanton, J. F., Koch, H., and Krylov, A. I., "Equation-of-motion coupled-cluster method with double electron-attaching operators: Theory, implementation, and benchmarks," *The Journal of Chemical Physics* **154**, 114115 (2021).
- <sup>39</sup>Halbert, L., Vidal, M. L., Shee, A., Coriani, S., and Severo Pereira Gomes, A., "Relativistic eom-ccsd for core-excited and core-ionized state energies based on the four-component dirac–coulomb (– gaunt) hamiltonian," *Journal of Chemical Theory and Computation* **17**, 3583–3598 (2021).
- <sup>40</sup>Helgaker, T., Coriani, S., Jørgensen, P., Kristensen, K., Olsen, J., and Ruud, K., "Recent advances in wave function-based methods of molecular-property calculations," *Chemical reviews* **112**, 543–631 (2012).

- <sup>41</sup>Herbst, M. F. and Fransson, T., "Quantifying the error of the core–valence separation approximation," *The Journal of Chemical Physics* **153**, 054114 (2020).
- <sup>42</sup>Hirata, S. and Head-Gordon, M., "Time-dependent density functional theory within the tamm–dancoff approximation," *Chemical Physics Letters* **314**, 291–299 (1999).
- <sup>43</sup>Höfener, S., Gomes, A. S. P., and Visscher, L., "Solvatochromic shifts from coupled-cluster theory embedded in density functional theory," *The Journal of Chemical Physics* **139**, 104106 (2013).
- <sup>44</sup>Höfener, S., Severo Pereira Gomes, A., and Visscher, L., "Molecular properties via a subsystem density functional theory formulation: A common framework for electronic embedding," *The Journal of chemical physics* **136**, 044104 (2012).
- <sup>45</sup>Hu, K.-Q., Huang, Z.-W., Zhang, Z.-H., Mei, L., Qian, B.-B., Yu, J.-P., Chai, Z.-F., and Shi, W.-Q., "Actinide-based porphyrinic mof as a dehydrogenation catalyst," *Chemistry–A European Journal* **24**, 16766–16769 (2018).
- <sup>46</sup>Hu, Y., Shen, Z., Li, B., Tan, X., Han, B., Ji, Z., Wang, J., Zhao, G., and Wang, X., "State-of-the-art progress for the selective crystallization of actinides, synthesis of actinide compounds and their functionalization," *Journal of Hazardous Materials* **426**, 127838 (2022).
- <sup>47</sup>Husar, R., Dumas, T., Schlegel, M. L., Schlegel, D., Guillaumont, D., Solari, P.-L., and Moisy, P., "X-ray absorption spectroscopy and actinide electrochemistry: a setup dedicated to radioactive samples applied to neptunium chemistry," *Journal of Synchrotron Radiation* **29** (2022).
- <sup>48</sup>Ilton, E. S. and Bagus, P. S., "Ligand field effects on the multiplet structure of the u4f xps of uo<sub>2</sub>," *Surface science* **602**, 1114–1121 (2008).
- <sup>49</sup>Ion, R.-M., Sorescu, A.-A., and Nuta, A., "Green synthesis of lanthanides and actinides-based nanomaterials," in *Handbook of Greener Synthesis of Nanomaterials and Compounds* (Elsevier, 2021) pp. 355–388.
- <sup>50</sup>Iwasawa, Y., Asakura, K., and Tada, M., *XAFS techniques for catalysts, nanomaterials, and surfaces* (Springer, 2017).
- <sup>51</sup>Jacob, C. R. and Neugebauer, J., "Subsystem density-functional theory," *Wiley Interdisciplinary Reviews: Computational Molecular Science* **4**, 325–362 (2014).
- <sup>52</sup>Ji, S., Su, M., Liao, C., Ma, S., Wang, Z., Shih, K., Chang, C.-K., Lee, J.-F., Chan, T.-S., and Li, Y., "Synchrotron x-ray spectroscopy investigation of the ca1- xlnxrti<sub>2</sub>- x (al, fe) x<sub>0.7</sub> zirconolite ceramics (ln= la, nd, gd, ho, yb)," *Journal of the American Ceramic Society* **103**, 1463–1475 (2020).
- <sup>53</sup>Jones, L. O., Mosquera, M. A., Schatz, G. C., and Ratner, M. A., "Embedding methods for quantum chemistry: applications from materials to life sciences," *Journal of the American Chemical Society* **142**, 3281–3295 (2020).
- <sup>54</sup>Karbowiak, M., Drozdzyński, J., Murdoch, K., Edelstein, N., and Hubert, S., "Spectroscopic studies and crystal-field analysis of u<sup>3+</sup> ions in rby<sub>2</sub>cl<sub>7</sub> single crystals," *The Journal of chemical physics* **106**, 3067–3077 (1997).
- <sup>55</sup>Kauczor, J. and Norman, P., "Efficient calculations of molecular linear response properties for spectral regions," *Journal of Chemical Theory and Computation* **10**, 2449–2455 (2014).
- <sup>56</sup>Konecny, L., Repisky, M., Ruud, K., and Komorovsky, S., "Relativistic four-component linear damped response tddft for electronic absorption and circular dichroism calculations," *The Journal of Chemical Physics* **151**, 194112 (2019).
- <sup>57</sup>Konecny, L., Vicha, J., Komorovsky, S., Ruud, K., and Repisky, M., "Accurate x-ray absorption spectra near l- and m-edges from relativistic four-component damped response time-dependent density functional theory," *Inorganic chemistry* (2021).
- <sup>58</sup>Kozioł, K. and Aucar, G. A., "Qed effects on individual atomic orbital energies," *The Journal of Chemical Physics* **148**, 134101 (2018).
- <sup>59</sup>Krause, M. and Oliver, J., "Naturcal wiciths of atomic k and l. levels, kor x-ray lines and several kii. auger lines," *J. Phys. Chem. Ref. Data* **8** (1979).
- <sup>60</sup>Krykunov, M. and Ziegler, T., "Self-consistent formulation of constricted variational density functional theory with orbital relaxation. implementation and applications," *Journal of Chemical Theory and Computation* **9**, 2761–2773 (2013).
- <sup>61</sup>Kvashnina, K., Kvashnin, Y., and Butorin, S., "Role of resonant inelastic x-ray scattering in high-resolution core-level spectroscopy of actinide materials," *Journal of Electron Spectroscopy and Related Phenomena* **194**, 27–36 (2014).
- <sup>62</sup>Kvashnina, K. O. and Butorin, S. M., "High-energy resolution x-ray spectroscopy at actinide m 4, 5 and ligand k edges: what we know, what we want to know, and what we can know," *Chemical Communications* **58**, 327–342 (2022).
- <sup>63</sup>van der Laan, G. and Figueroa, A. I., "X-ray magnetic circular dichroism—a versatile tool to study magnetism," *Coordination Chemistry Reviews* **277**, 95–129 (2014).
- <sup>64</sup>Leduc, J., Frank, M., Jürgensen, L., Graf, D., Raauf, A., and Mathur, S., "Chemistry of actinide centers in heterogeneous catalytic transformations of small molecules," *ACS Catalysis* **9**, 4719–4741 (2019).
- <sup>65</sup>Lindroth, E., Calegari, F., Young, L., Harmand, M., Dudovich, N., Berrah, N., and Smirnova, O., "Challenges and opportunities in attosecond and xfel science," *Nature Reviews Physics* **1**, 107–111 (2019).
- <sup>66</sup>Lischka, H., Nachtigallova, D., Aquino, A. J., Szalay, P. G., Plasser, F., Machado, F. B., and Barbatti, M., "Multireference approaches for excited states of molecules," *Chemical reviews* **118**, 7293–7361 (2018).
- <sup>67</sup>Liu, W., "Essentials of relativistic quantum chemistry," *The Journal of chemical physics* **152**, 180901 (2020).
- <sup>68</sup>Lv, B., Qian, T., and Ding, H., "Angle-resolved photoemission spectroscopy and its application to topological materials," *Nature Reviews Physics* **1**, 609–626 (2019).
- <sup>69</sup>Martin, R. L., "Natural transition orbitals," *The Journal of chemical physics* **118**, 4775–4777 (2003).
- <sup>70</sup>Mathur, J., Murali, M., and Nash, K., "Actinide partitioning—a review," *Solvent extraction and ion exchange* **19**, 357–390 (2001).
- <sup>71</sup>McSkimming, A., Su, J., Cheisson, T., Gau, M. R., Carroll, P. J., Batista, E. R., Yang, P., and Schelter, E. J., "Coordination chemistry of a strongly-donating hydroxylamine with early actinides: An investigation of redox properties and electronic structure," *Inorganic Chemistry* **57**, 4387–4394 (2018).
- <sup>72</sup>Van der Meeren, A., Angulo, J. F., Bohand, S., and Griffiths, N. M., "A quick and simple in vitro assay to predict bioavailability of actinides following accidental exposure," *Toxicology in Vitro* **58**, 142–149 (2019).
- <sup>73</sup>Minasian, S. G., Keith, J. M., Batista, E. R., Boland, K. S., Clark, D. L., Conradson, S. D., Kozimor, S. A., Martin, R. L., Schwarz, D. E., Shuh, D. K., *et al.*, "Determining relative f and d orbital contributions to m–cl covalency in mcl<sub>6</sub>2–(m= ti, zr, hf, u) and uocl<sub>5</sub>—using cl k-edge x-ray absorption spectroscopy and time-dependent density functional theory," *Journal of the American Chemical Society* **134**, 5586–5597 (2012).
- <sup>74</sup>Misael, W. A. and Gomes, A. S. P., "Dataset: Core excitations and ionizations of uranyl in cs<sub>2</sub>uo<sub>2</sub>cl<sub>4</sub> from relativistic embedded damped response time-dependent density functional theory and equation of motion coupled cluster calculations," <https://doi.org/10.5281/zenodo.7632750>.
- <sup>75</sup>Nocton, G. and Mazzanti, M., "Coordination chemistry of actinides," *Lanthanides And Actinides, The: Synthesis, Reactivity, Properties And Applications*, 149 (2021).
- <sup>76</sup>Norman, P., "A perspective on nonresonant and resonant electronic response theory for time-dependent molecular properties," *Physical chemistry chemical physics* **13**, 20519–20535 (2011).
- <sup>77</sup>Norman, P. and Ågren, H., "Geometry optimization of core electron excited molecules," *Journal of Molecular Structure: THEOCHEM* **401**, 107–115 (1997).
- <sup>78</sup>Norman, P. and Dreuw, A., "Simulating x-ray spectroscopies and calculating core-excited states of molecules," *Chemical reviews*

- 118, 7208–7248 (2018).
- <sup>79</sup>Norman, P., Ruud, K., and Saue, T., *Principles and practices of molecular properties: Theory, modeling, and simulations* (John Wiley & Sons, 2018).
- <sup>80</sup>Ogasawara, H., Kotani, A., and Thole, B. T., “Calculation of magnetic x-ray dichroism in 4d and 5d absorption spectra of actinides,” *Physical Review B* **44**, 2169 (1991).
- <sup>81</sup>Oher, H., Ferru, G., Couston, L., Berthon, L., Guillaumont, D., Réal, F., Vercouter, T., and Vallet, V., “Influence of the first coordination of uranyl on its luminescence properties: A study of uranyl binitrate with n, n-dialkyl amide dehiba and water,” *Inorganic Chemistry* **61**, 890–901 (2021).
- <sup>82</sup>Oher, H., Réal, F., Vercouter, T., and Vallet, V., “Investigation of the luminescence of [uo2x4] 2-(x= cl, br) complexes in the organic phase using time-resolved laser-induced fluorescence spectroscopy and quantum chemical simulations,” *Inorganic Chemistry* **59**, 5896–5906 (2020).
- <sup>83</sup>Oher, H., Vercouter, T., Réal, F., Shang, C., Reiller, P. E., and Vallet, V., “Influence of alkaline earth metal ions on structures and luminescent properties of na m m n uo2 (co3) 3 (4-m-2 n)-(m= mg, ca; m, n= 0-2): Time-resolved fluorescence spectroscopy and ab initio studies,” *Inorganic Chemistry* **59**, 15036–15049 (2020).
- <sup>84</sup>Pallares, R. M. and Abergel, R. J., “Transforming lanthanide and actinide chemistry with nanoparticles,” *Nanoscale* **12**, 1339–1348 (2020).
- <sup>85</sup>Park, J. W., Al-Saadon, R., MacLeod, M. K., Shiozaki, T., and Vlasisavljevich, B., “Multireference electron correlation methods: Journeys along potential energy surfaces,” *Chemical Reviews* **120**, 5878–5909 (2020).
- <sup>86</sup>Parker, B., Zhang, Z., Rao, L., and Arnold, J., “An overview and recent progress in the chemistry of uranium extraction from seawater,” *Dalton Transactions* **47**, 639–644 (2018).
- <sup>87</sup>Parmar, P., Samuels, A., and Clark, A. E., “Applications of polarizable continuum models to determine accurate solution-phase thermochemical values across a broad range of cation charge—the case of u (iii–vi),” *Journal of chemical theory and computation* **11**, 55–63 (2015).
- <sup>88</sup>Pavlyuk, A. O., Kotlyarevskii, S. G., Kan, R. I., Volkova, A. G., Yapaskurt, V. O., Zakharova, E. V., and Shiryaev, A. A., “Actinides and fission products in reactor graphite after loss-of-flow accident,” *npj Materials Degradation* **6**, 23 (2022).
- <sup>89</sup>Pavošević, F., Rousseau, B. J., and Hammes-Schiffer, S., “Multi-component orbital-optimized perturbation theory methods: Approaching coupled cluster accuracy at lower cost,” *The Journal of Physical Chemistry Letters* **11**, 1578–1583 (2020).
- <sup>90</sup>Pidchenko, I., Kvashnina, K. O., Yokosawa, T., Finck, N., Bahl, S., Schild, D., Polly, R., Bohnert, E., Rossberg, A., Göttlicher, J., *et al.*, “Uranium redox transformations after u (vi) coprecipitation with magnetite nanoparticles,” *Environmental science & technology* **51**, 2217–2225 (2017).
- <sup>91</sup>Polly, R., Schacherl, B., Rothe, J., and Vitova, T., “Relativistic multiconfigurational ab initio calculation of uranyl 3d4f resonant inelastic x-ray scattering,” *Inorganic chemistry* **60**, 18764–18776 (2021).
- <sup>92</sup>Popa, K., Prieur, D., Manara, D., Naji, M., Vigier, J.-F., Martin, P. M., Blanco, O. D., Scheinost, A. C., Prüßmann, T., Vitova, T., *et al.*, “Further insights into the chemistry of the bi-u-o system,” *Dalton Transactions* **45**, 7847–7855 (2016).
- <sup>93</sup>Pyykkö, P., “Relativistic quantum chemistry,” in *Advances in quantum chemistry*, Vol. 11 (Elsevier, 1978) pp. 353–409.
- <sup>94</sup>Ramanantoanina, H., “On the calculation of multiplet energies of three-open-shell 4f 13 5f n 6d 1 electron configuration by lfdft: modeling the optical spectra of 4f core-electron excitation in actinide compounds,” *Physical Chemistry Chemical Physics* **19**, 32481–32491 (2017).
- <sup>95</sup>Ramanantoanina, H., Kuri, G., Daul, C., and Bertsch, J., “Core electron excitations in u 4+: modelling of the nd 10 5f 2→nd 9 5f 3 transitions with n= 3, 4 and 5 by ligand field tools and density functional theory,” *Physical Chemistry Chemical Physics* **18**, 19020–19031 (2016).
- <sup>96</sup>Ramanantoanina, H., Kuri, G., Martin, M., and Bertsch, J., “Study of electronic structure in the l-edge spectroscopy of actinide materials: Uo 2 as an example,” *Physical Chemistry Chemical Physics* **21**, 7789–7801 (2019).
- <sup>97</sup>Réal, F., Vallet, V., Marian, C., and Wahlgren, U., “Theoretical investigation of the energies and geometries of photoexcited uranyl (vi) ion: A comparison between wave-function theory and density functional theory,” *The Journal of chemical physics* **127**, 214302 (2007).
- <sup>98</sup>Reiher, M. and Wolf, A., *Relativistic quantum chemistry: the fundamental theory of molecular science* (John Wiley & Sons, 2014).
- <sup>99</sup>Rothe, J., Altmaier, M., Dagan, R., Dardenne, K., Fellhauer, D., Gaona, X., González-Robles Corrales, E., Herm, M., Kvashnina, K. O., Metz, V., *et al.*, “Fifteen years of radionuclide research at the kit synchrotron source in the context of the nuclear waste disposal safety case,” *Geosciences* **9**, 91 (2019).
- <sup>100</sup>Saue, T., “Relativistic hamiltonians for chemistry: A primer,” *ChemPhysChem* **12**, 3077–3094 (2011).
- <sup>101</sup>Saue, T., Bast, R., Gomes, A. S. P., Jensen, H. J. A., Visscher, L., Aucar, I. A., Di Remigio, R., Dyall, K. G., Eliav, E., Fasshauer, E., *et al.*, “The dirac code for relativistic molecular calculations,” *The Journal of chemical physics* **152**, 204104 (2020).
- <sup>102</sup>Scheinost, A. C., Claussner, J., Exner, J., Feig, M., Findeisen, S., Hennig, C., Kvashnina, K. O., Naudet, D., Prieur, D., Rossberg, A., *et al.*, “Robl-ii at esrf: a synchrotron toolbox for actinide research,” *Journal of Synchrotron Radiation* **28**, 333–349 (2021).
- <sup>103</sup>Sedigh Rahimabadi, P., Khodaei, M., and Koswattage, K. R., “Review on applications of synchrotron-based x-ray techniques in materials characterization,” *X-Ray Spectrometry* **49**, 348–373 (2020).
- <sup>104</sup>Sen, S., Shee, A., and Mukherjee, D., “Inclusion of orbital relaxation and correlation through the unitary group adapted open shell coupled cluster theory using non-relativistic and scalar relativistic hamiltonians to study the core ionization potential of molecules containing light to medium-heavy elements,” *The Journal of Chemical Physics* **148**, 054107 (2018).
- <sup>105</sup>Sergentu, D.-C. and Autschbach, J., “X-ray absorption spectra of f-element complexes: insight from relativistic multiconfigurational wavefunction theory,” *Dalton Transactions* (2022).
- <sup>106</sup>Sergentu, D.-C., Duignan, T. J., and Autschbach, J., “Ab initio study of covalency in the ground versus core-excited states and x-ray absorption spectra of actinide complexes,” *The Journal of Physical Chemistry Letters* **9**, 5583–5591 (2018).
- <sup>107</sup>Shi, W.-Q., Yuan, L.-Y., Wang, C.-Z., Wang, L., Mei, L., Xiao, C.-L., Zhang, L., Li, Z.-J., Zhao, Y.-L., and Chai, Z.-F., “Exploring actinide materials through synchrotron radiation techniques,” *Synchrotron Radiation in Materials Science: Light Sources, Techniques, and Applications* **2**, 389–509 (2018).
- <sup>108</sup>Sikkema, J., Visscher, L., Saue, T., and Iliaš, M., “The molecular mean-field approach for correlated relativistic calculations,” *The Journal of chemical physics* **131**, 124116 (2009).
- <sup>109</sup>Skripnikov, L. V., Chubukov, D. V., and Shakhova, V. M., “The role of qed effects in transition energies of heavy-atom alkaline earth monofluoride molecules: A theoretical study of ba+, baf, raf, and e12of,” *The Journal of Chemical Physics* **155**, 144103 (2021).
- <sup>110</sup>South, C., Shee, A., Mukherjee, D., Wilson, A. K., and Saue, T., “4-component relativistic calculations of l 3 ionization and excitations for the isoelectronic species uo 2 2+, oun+ and un 2,” *Physical Chemistry Chemical Physics* **18**, 21010–21023 (2016).
- <sup>111</sup>Southworth, S., Dunford, R., Ray, D., Kanter, E., Doumy, G., March, A., Ho, P., Krässig, B., Gao, Y., Lehmann, C., *et al.*, “Observing pre-edge k-shell resonances in kr, xe, and xef 2,” *Physical Review A* **100**, 022507 (2019).
- <sup>112</sup>Stener, M., Fronzoni, G., and de Simone, M. d., “Time dependent density functional theory of core electrons excitations,”

- Chemical physics letters **373**, 115–123 (2003).
- <sup>113</sup>Stöhr, J., *NEXAFS spectroscopy*, Vol. 25 (Springer Science & Business Media, 1992).
- <sup>114</sup>Stöhr, J., “What are x-rays, anyway: A modern view of the nature of light and its implications for the future of x-ray science,” (2019).
- <sup>115</sup>Te Velde, G. t., Bickelhaupt, F. M., Baerends, E. J., Fonseca Guerra, C., van Gisbergen, S. J., Snijders, J. G., and Ziegler, T., “Chemistry with adf,” *Journal of Computational Chemistry* **22**, 931–967 (2001).
- <sup>116</sup>Tecmer, P., Bast, R., Ruud, K., and Visscher, L., “Charge-transfer excitations in uranyl tetrachloride ([ $\text{UO}_2\text{Cl}_4$ ]  $2^-$ ): How reliable are electronic spectra from relativistic time-dependent density functional theory?” *The Journal of Physical Chemistry A* **116**, 7397–7404 (2012).
- <sup>117</sup>Thiel, W. and Hummer, G., “Methods for computational chemistry,” *Nature* **504**, 96–97 (2013).
- <sup>118</sup>Thouvenot, P., Hubert, S., and Edelstein, N., “Spectroscopic study and crystal-field analysis of  $\text{cm } 3+$  in the cubic-symmetry site of  $\text{tho } 2$ ,” *Physical Review B* **50**, 9715 (1994).
- <sup>119</sup>Tobin, J., Ramanantoanina, H., Daul, C., Roussel, P., Yu, S.-W., Nowak, S., Alonso-Mori, R., Kroll, T., Nordlund, D., Weng, T.-C., *et al.*, “Unoccupied electronic structure of actinide dioxides,” *Physical Review B* **105**, 125129 (2022).
- <sup>120</sup>Trivikram, T. M., Schlösser, M., Ubachs, W., and Salumbides, E., “Relativistic and qed effects in the fundamental vibration of  $\text{t } 2$ ,” *Physical Review Letters* **120**, 163002 (2018).
- <sup>121</sup>Vallejo, K. D., Kabir, F., Poudel, N., Marianetti, C., Hurley, D. H., Simmonds, P., Dennett, C. A., and Gofryk, K., “Advances in actinide thin films: synthesis, properties, and future directions,” *Reports on Progress in Physics* (2022).
- <sup>122</sup>Van Bokhoven, J. A. and Lamberti, C., *X-ray absorption and X-ray emission spectroscopy: theory and applications*, Vol. 1 (John Wiley & Sons, 2016).
- <sup>123</sup>Van Lenthe, E. and Baerends, E. J., “Optimized slater-type basis sets for the elements 1–118,” *Journal of computational chemistry* **24**, 1142–1156 (2003).
- <sup>124</sup>Van Lenthe, E. v., Snijders, J., and Baerends, E., “The zero-order regular approximation for relativistic effects: The effect of spin-orbit coupling in closed shell molecules,” *The Journal of chemical physics* **105**, 6505–6516 (1996).
- <sup>125</sup>Velisek-Carolan, J., “Separation of actinides from spent nuclear fuel: A review,” *Journal of hazardous materials* **318**, 266–281 (2016).
- <sup>126</sup>Vidal, M. L., Feng, X., Epifanovsky, E., Krylov, A. I., and Coriani, S., “New and efficient equation-of-motion coupled-cluster framework for core-excited and core-ionized states,” *Journal of Chemical Theory and Computation* **15**, 3117–3133 (2019).
- <sup>127</sup>Vidal, M. L., Pokhilko, P., Krylov, A. I., and Coriani, S., “Equation-of-motion coupled-cluster theory to model l-edge x-ray absorption and photoelectron spectra,” *The journal of physical chemistry letters* **11**, 8314–8321 (2020).
- <sup>128</sup>Villaume, S., Saue, T., and Norman, P., “Linear complex polarization propagator in a four-component kohn–sham framework,” *The Journal of chemical physics* **133**, 064105 (2010).
- <sup>129</sup>Visscher, L., “Approximate molecular relativistic dirac-coulomb calculations using a simple coulombic correction,” *Theoretical Chemistry Accounts* **98**, 68–70 (1997).
- <sup>130</sup>Visscher, L. and Dyall, K. G., “Dirac–fock atomic electronic structure calculations using different nuclear charge distributions,” *Atomic Data and Nuclear Data Tables* **67**, 207–224 (1997).
- <sup>131</sup>Vitova, T., Denecke, M., Göttlicher, J., Jorissen, K., Kas, J., Kvashnina, K., Prüßmann, T., Rehr, J., and Rothe, J., “Actinide and lanthanide speciation with high-energy resolution x-ray techniques,” in *Journal of Physics: Conference Series*, Vol. 430 (IOP Publishing, 2013) p. 012117.
- <sup>132</sup>Vitova, T., Green, J. C., Denning, R. G., Löble, M., Kvashnina, K., Kas, J. J., Jorissen, K., Rehr, J. J., Malcherek, T., and Denecke, M. A., “Polarization dependent high energy resolution x-ray absorption study of dicesium uranyl tetrachloride,” *Inorganic chemistry* **54**, 174–182 (2015).
- <sup>133</sup>Vitova, T., Kvashnina, K., Nocton, G., Sukharina, G., Denecke, M., Butorin, S., Mazzanti, M., Caciuffo, R., Soldatov, A., Behrends, T., *et al.*, “High energy resolution x-ray absorption spectroscopy study of uranium in varying valence states,” *Physical Review B* **82**, 235118 (2010).
- <sup>134</sup>Vitova, T., Pidchenko, I., Fellhauer, D., Bagus, P. S., Joly, Y., Pruessmann, T., Bahl, S., Gonzalez-Robles, E., Rothe, J., Altmaier, M., *et al.*, “The role of the 5f valence orbitals of early actinides in chemical bonding,” *Nature communications* **8**, 1–9 (2017).
- <sup>135</sup>Vitova, T., Pidchenko, I., Fellhauer, D., Pruessmann, T., Bahl, S., Dardenne, K., Yokosawa, T., Schimmelpfennig, B., Altmaier, M., Denecke, M., *et al.*, “Exploring the electronic structure and speciation of aqueous and colloidal pu with high energy resolution xanes and computations,” *Chemical Communications* **54**, 12824–12827 (2018).
- <sup>136</sup>Watkin, D. J., Denning, R. G., and Prout, K., “Structure of dicaesium tetrachlorodioxouranium (vi),” *Acta Crystallographica Section C: Crystal Structure Communications* **47**, 2517–2519 (1991).
- <sup>137</sup>Wenzel, J., Holzer, A., Wormit, M., and Dreuw, A., “Analysis and comparison of cvs-adc approaches up to third order for the calculation of core-excited states,” *The Journal of Chemical Physics* **142**, 214104 (2015).
- <sup>138</sup>Wernet, P., “Chemical interactions and dynamics with femtosecond x-ray spectroscopy and the role of x-ray free-electron lasers,” *Philosophical Transactions of the Royal Society A* **377**, 20170464 (2019).
- <sup>139</sup>Wesolowski, T. A., Shedje, S., and Zhou, X., “Frozen-density embedding strategy for multilevel simulations of electronic structure,” *Chemical reviews* **115**, 5891–5928 (2015).
- <sup>140</sup>Wesolowski, T. A. and Warshel, A., “Frozen density functional approach for ab initio calculations of solvated molecules,” *The Journal of Physical Chemistry* **97**, 8050–8053 (1993).
- <sup>141</sup>Willmott, P., *An introduction to synchrotron radiation: techniques and applications* (John Wiley & Sons, 2019).
- <sup>142</sup>Yanai, T., Tew, D. P., and Handy, N. C., “A new hybrid exchange–correlation functional using the coulomb-attenuating method (cam-b3lyp),” *Chemical physics letters* **393**, 51–57 (2004).
- <sup>143</sup>Zegke, M., Zhang, X., Pidchenko, I., Hlina, J. A., Lord, R. M., Purkis, J., Nichol, G. S., Magnani, N., Schreckenbach, G., Vitova, T., *et al.*, “Differential uranyl (v) oxo-group bonding between the uranium and metal cations from groups 1, 2, 4, and 12; a high energy resolution x-ray absorption, computational, and synthetic study,” *Chemical science* **10**, 9740–9751 (2019).
- <sup>144</sup>Zhai, B., Tian, Q., Li, N., Yan, M., and Henderson, M. J., “Saxs study of the formation and structure of polynuclear thorium (iv) colloids and thorium dioxide nanoparticles,” *Journal of Synchrotron Radiation* **29** (2022).
- <sup>145</sup>Zhang, Y., Biggs, J. D., Healion, D., Govind, N., and Mukamel, S., “Core and valence excitations in resonant x-ray spectroscopy using restricted excitation window time-dependent density functional theory,” *The Journal of chemical physics* **137**, 194306 (2012).
- <sup>146</sup>Zheng, X. and Cheng, L., “Performance of delta-coupled-cluster methods for calculations of core-ionization energies of first-row elements,” *Journal of chemical theory and computation* **15**, 4945–4955 (2019).
- <sup>147</sup>Zimina, A., Dardenne, K., Denecke, M. A., Grunwaldt, J., Huttel, E., Lichtenberg, H., Mangold, S., Pruessmann, T., Rothe, J., Steininger, R., *et al.*, “The cat-act beamline at anka: A new high energy x-ray spectroscopy facility for catalysis and actinide research,” in *Journal of Physics: Conference Series*, Vol. 712 (IOP Publishing, 2016) p. 012019.

**Supplementary Information to "Core excitations and ionizations of uranyl in  $\text{Cs}_2\text{UO}_2\text{Cl}_4$  from relativistic embedded damped response time-dependent density functional theory and equation of motion coupled cluster calculations"**

Wilken Aldair Misael<sup>a)</sup> and André Severo Pereira Gomes<sup>b)</sup>

*Univ. Lille, CNRS, UMR 8523-PhLAM-Physique des Lasers Atomes et Molécules,  
F-59000 Lille, France*

(Dated: 21 February 2023)

---

<sup>a)</sup>Electronic mail: wilken.misael@univ-lille.fr

<sup>b)</sup>Author to whom correspondence should be addressed; Electronic mail: andre.gomes@univ-lille.fr

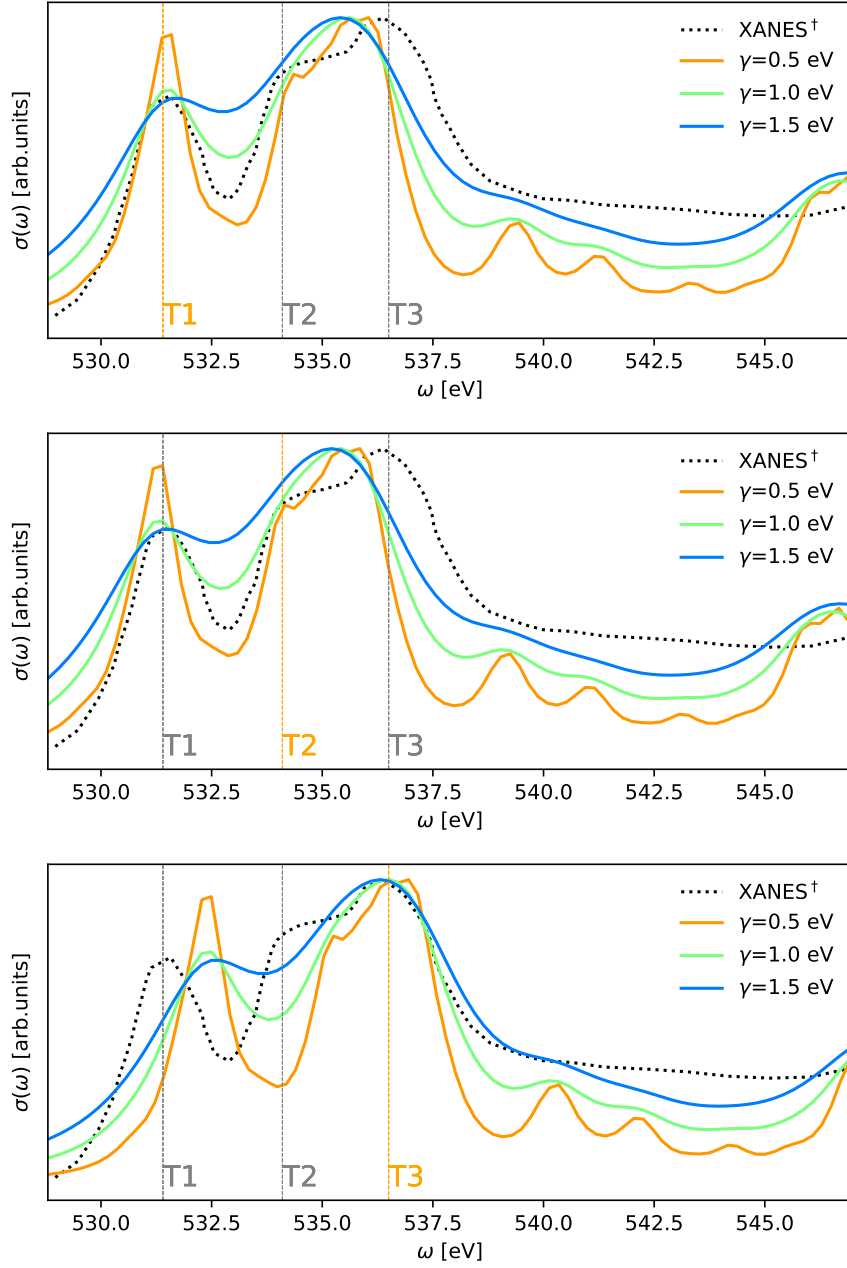


FIG. 1: Comparison for 4c-DR-TD-CAMB3LYP XAS spectra at the oxygen K-edge for different damping factors and shifts (depicted as the orange straight line) with respect to the experimental data ( $\text{Cs}_2\text{UO}_2\text{Cl}_4$ ) from Denning *et al.*<sup>3</sup>

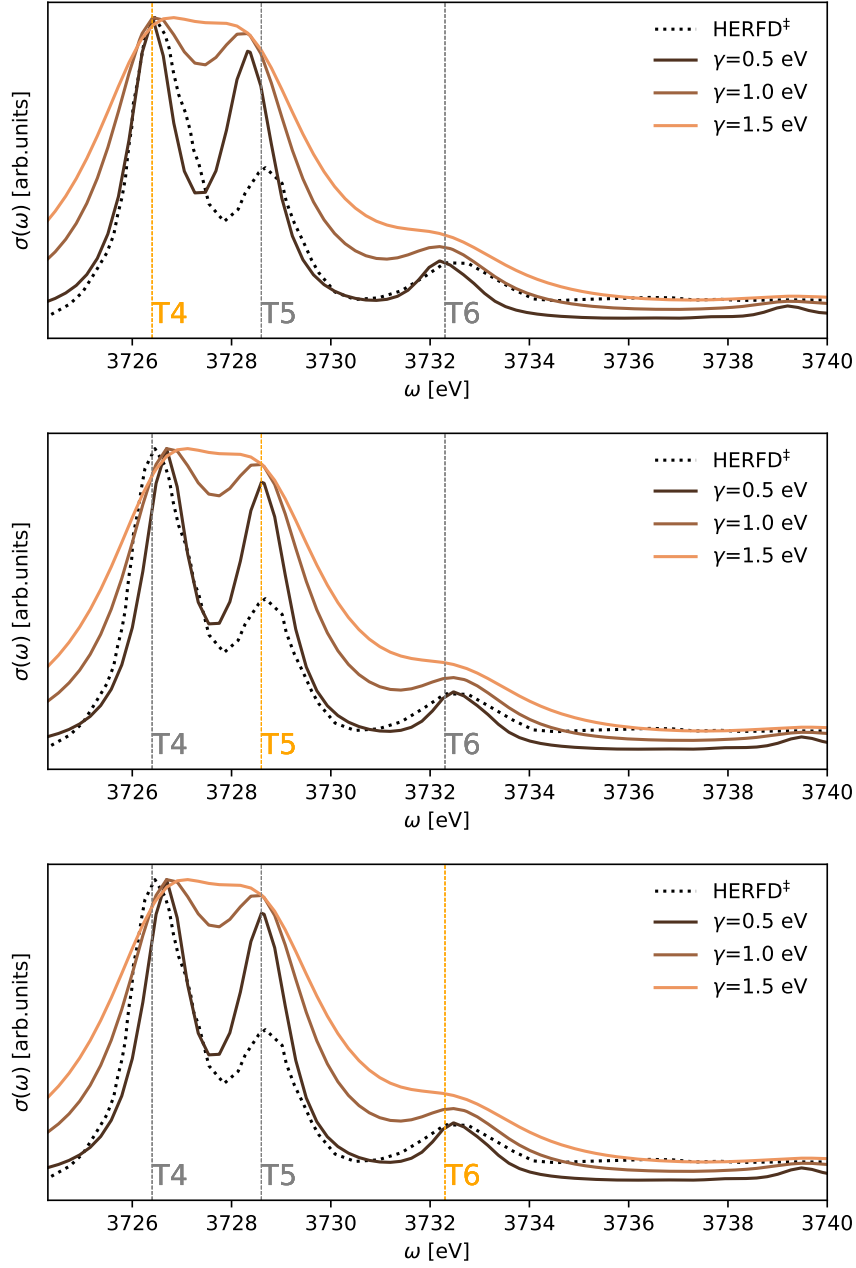


FIG. 2: Comparison for 4c-DR-TD-CAMB3LYP XAS spectra at the uranium  $M_4$ -edge for different damping factors and shifts (depicted as the orange straight line) with respect to the experimental data ( $\text{Cs}_2\text{UO}_2\text{Cl}_4$ ) from Vitova *et al.*<sup>6</sup>

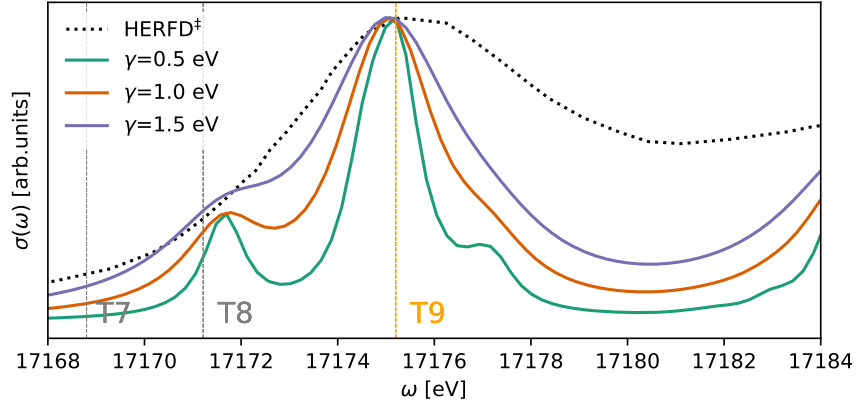
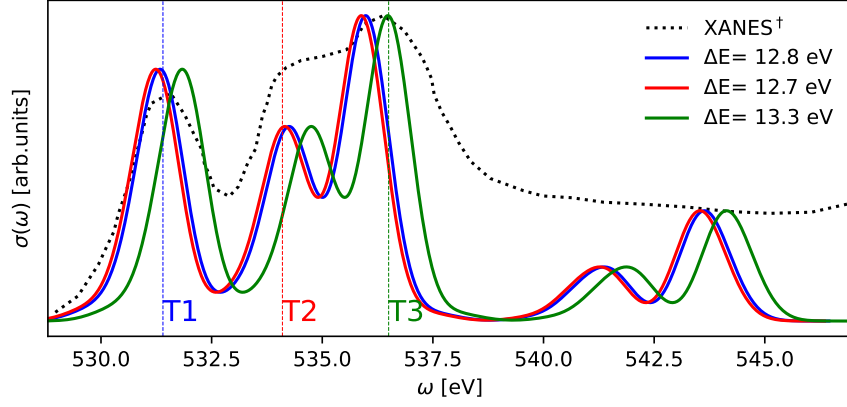
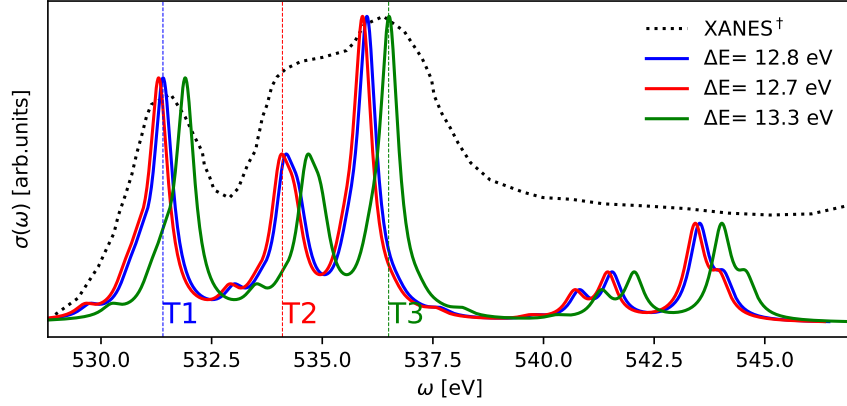


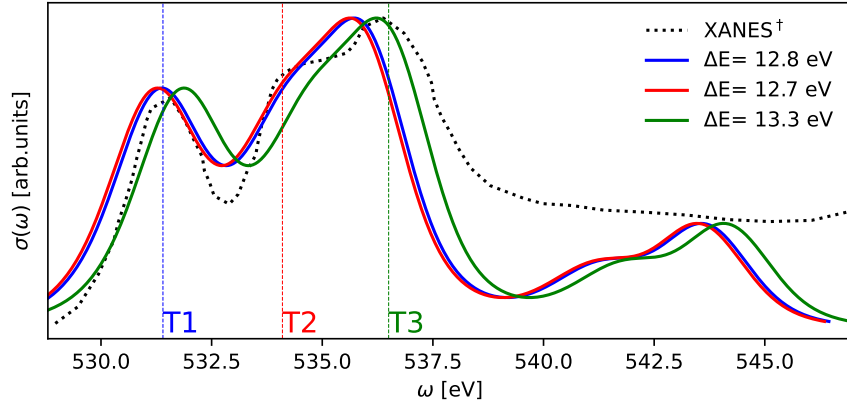
FIG. 3: Comparison for 4c-DR-TD-CAMB3LYP XAS spectra at the uranium  $L_3$ -edge for different damping factors. Shift (depicted as the orange straight line) with respect to the experimental data ( $\text{Cs}_2\text{UO}_2\text{Cl}_4$ ) from Vitova *et al.*<sup>6</sup>



(a) Gaussian function.

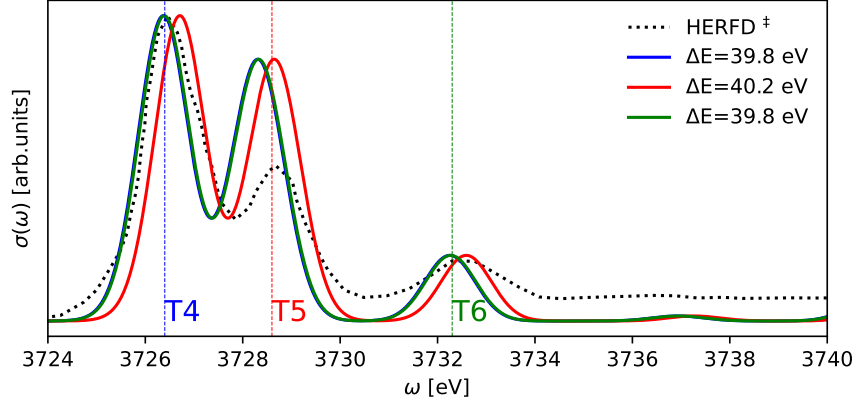


(b) Lorentzian function.

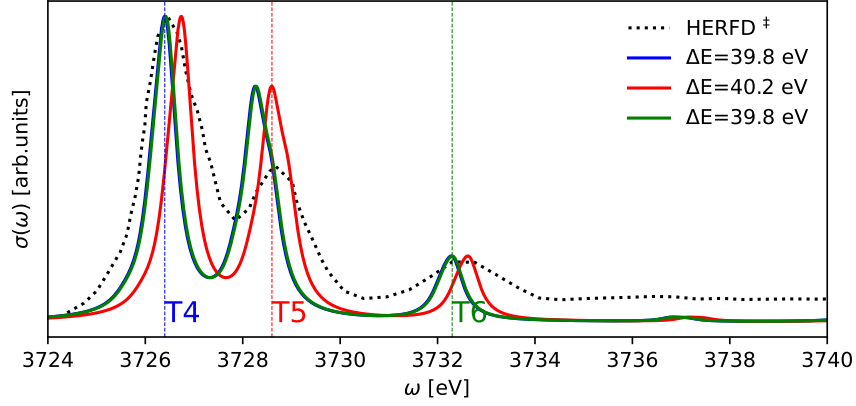


(c) Voigt function.

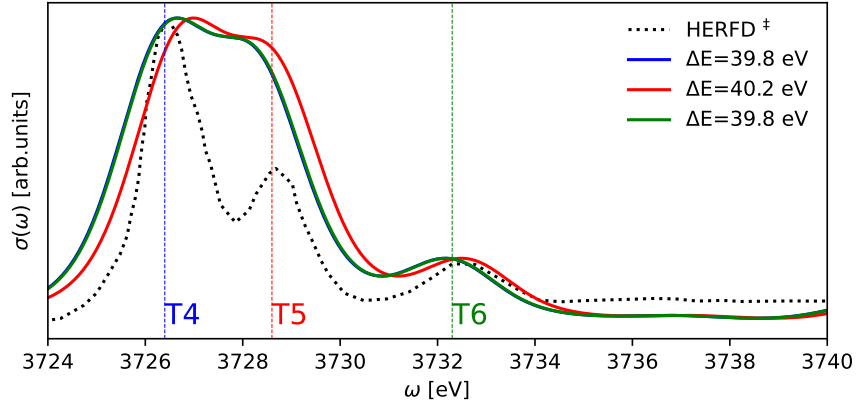
FIG. 4: Comparison for 2c-TDA-TD-CAMB3LYP XAS spectra at the oxygen K-edge for different broadening function and shifts (depicted as the coloured straight line) with respect to the experimental data ( $\text{Cs}_2\text{UO}_2\text{Cl}_4$ ) from Denning *et al.*<sup>3</sup>



(a) Gaussian function.

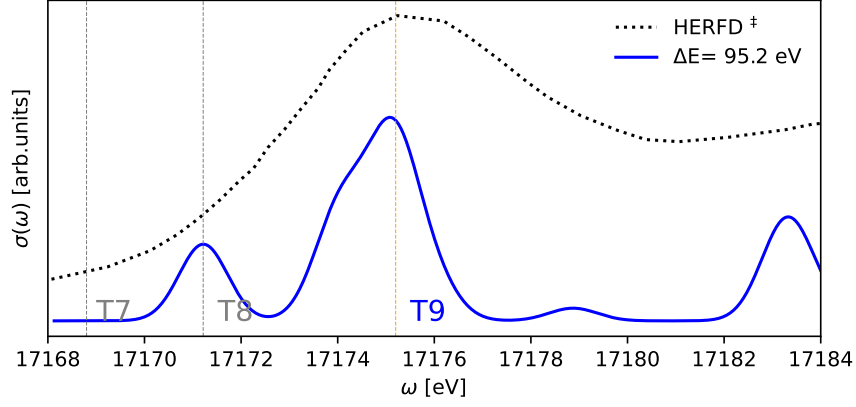


(b) Lorentzian function.

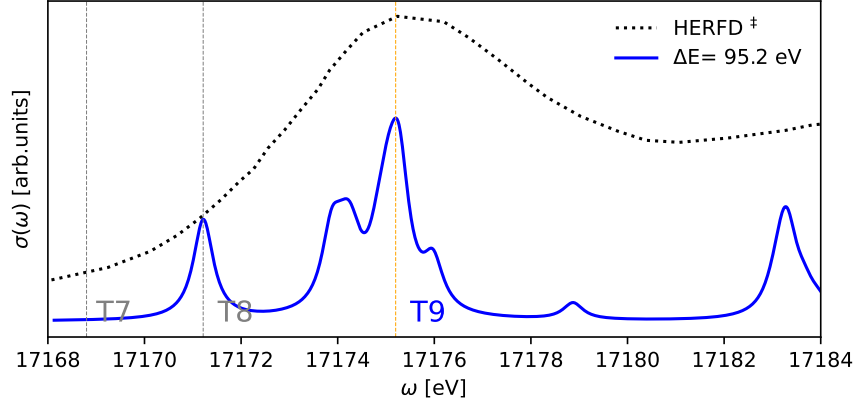


(c) Voigt function.

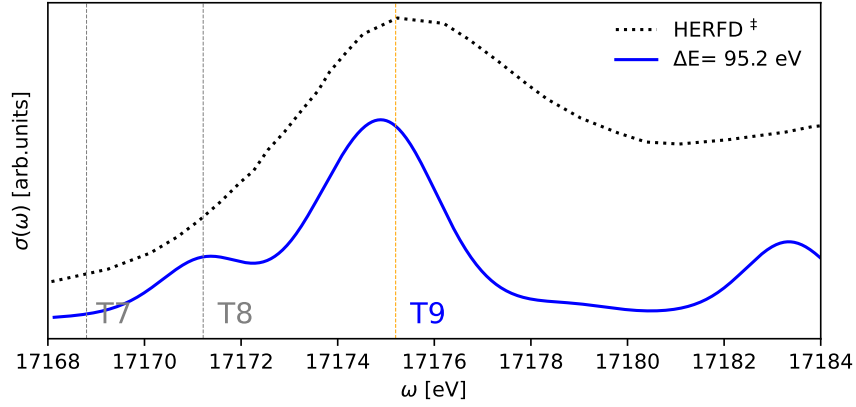
FIG. 5: Comparison for 2c-TDA-TD-CAMB3LYP XAS spectra at the uranium  $M_4$ -edge for different broadening functions and shifts (depicted as the colored straight line) with respect to the experimental data ( $\text{Cs}_2\text{UO}_2\text{Cl}_4$ ) from Vitova *et al.*<sup>6</sup>



(a) Gaussian function.



(b) Lorentzian function.



(c) Voigt function.

FIG. 6: Comparison for 2c-TDA-TD-CAMB3LYP XAS spectra at the uranium  $L_3$ -edge for different broadening functions with respect to the experimental data ( $\text{Cs}_2\text{UO}_2\text{Cl}_4$ ) from Vitova *et al.*<sup>6</sup>. Shift to the main line in the experiment, depicted as the orange straight line.

TABLE I: The difference in CVS-EOM-CCSD core ionization potentials and Koopmans' for the same Hamiltonian (in eV) for  $\text{UO}_2^{2+}$  using uncontracted Dyall double-zeta basis set for all atoms.

Atom	Assignment	$^4\text{DC}$	$^4\text{DC}(\text{SS} \text{SS})$	$^2\text{DC}^M$	$^2\text{DC}^M(\text{SS} \text{SS})$	$^2\text{DCG}^M$	$^2\text{DCG}^M(\text{SS} \text{SS})$
U	K	102.96	104.18	105.37	105.31	105.09	104.96
	L <sub>1</sub>	66.68	66.72	66.81	66.74	66.90	67.20
	L <sub>2</sub>	70.31	70.32	70.28	70.18	70.15	70.16
	L <sub>3</sub>	65.58	65.53	65.67	65.75	65.61	65.64
	M <sub>1</sub>	38.98	38.87	38.98	38.86	38.87	39.00
	M <sub>2</sub>	41.48	41.50	41.46	41.48	41.43	41.42
	M <sub>3</sub>	38.37	38.39	38.39	38.41	38.44	38.45
	M <sub>4</sub>	41.15	41.21	41.13	41.18	41.13	41.18
	M <sub>5</sub>	41.09	41.03	41.14	41.08	41.08	41.20
	N <sub>1</sub>	20.97	20.98	20.96	20.98	20.90	20.92
	N <sub>2</sub>	21.75	21.70	21.75	21.69	21.62	21.56
	N <sub>3</sub>	20.08	20.04	20.08	20.05	20.01	19.97
	N <sub>4</sub>	19.92	19.95	19.92	19.94	19.88	19.90
	N <sub>5</sub>	19.70	19.71	19.70	19.71	19.79	19.80
	N <sub>6</sub>	19.53	19.58	19.53	19.57	19.56	19.51
	N <sub>7</sub>	19.45	19.35	19.45	19.36	19.42	19.47
O	K	19.19	19.18	19.19	19.18	19.03	19.02

TABLE II: CVS-EOM-CCSD core ionization potentials (in eV) for  $\text{UO}_2^{2+}$  using uncontracted Dyall double-zeta basis set for all atoms when a different percentage of orbitals is included in the correlation space. All calculations were performed with the  ${}^2\text{DC}^M$  Hamiltonian.

Atom Assignment		Percentage of correlated orbitals					
		56.7	61.4	62.5	67.6	72.5	100
U	K	115946.16	115933.42	115933.30	115919.57	115912.85	115907.66
	L <sub>1</sub>	21852.81	21845.60	21845.46	21841.79	21840.63	21840.98
	L <sub>2</sub>	21001.04	20993.71	20993.48	20988.46	20987.21	20987.93
	L <sub>3</sub>	17199.16	17192.96	17192.78	17188.76	17187.96	17188.54
	M <sub>1</sub>	5597.32	5596.33	5596.34	5596.19	5596.16	5596.34
	M <sub>2</sub>	5219.68	5218.33	5218.21	5217.93	5218.00	5218.26
	M <sub>3</sub>	4335.98	4335.10	4335.03	4334.84	4334.91	4335.11
	M <sub>4</sub>	3756.98	3755.70	3755.81	3755.74	3756.01	3756.08
	M <sub>5</sub>	3579.05	3577.87	3577.81	3577.92	3578.17	3578.22
	N <sub>1</sub>	1477.54	1477.57	1477.56	1477.58	1477.57	1477.63
	N <sub>2</sub>	1308.15	1308.05	1308.06	1308.08	1308.13	1308.20
	N <sub>3</sub>	1075.81	1075.82	1075.81	1075.84	1075.87	1075.93
	N <sub>4</sub>	810.09	810.11	810.19	810.23	810.32	810.34
	N <sub>5</sub>	767.00	767.02	767.02	767.15	767.24	767.25
	N <sub>6</sub>	416.59	416.60	416.60	416.57	416.56	416.55
	N <sub>7</sub>	405.66	405.67	405.65	405.64	405.62	405.62
O	K	555.15	555.37	555.37	555.40	555.40	555.41

TABLE III: The difference in CVS-EOM-CCSD core ionization potentials (in eV) for  $\text{UO}_2^{2+}$  using uncontracted Dyall double-zeta basis set for all atoms from a calculation in which all orbitals are included in the correlation space. All calculations were performed with the  ${}^2\text{DC}^M$  Hamiltonian.

Atom Assignment		Percentage of correlated orbitals				
		56.7	61.4	62.5	67.6	72.5
U	K	38.50	25.76	25.64	11.91	5.19
	L <sub>1</sub>	4.61	4.47	0.80	-0.35	0.00
	L <sub>2</sub>	5.78	5.56	0.53	-0.71	0.00
	L <sub>3</sub>	10.62	4.42	4.24	0.22	-0.58
	M <sub>1</sub>	0.98	0.00	0.00	-0.14	-0.18
	M <sub>2</sub>	1.42	0.07	-0.05	-0.33	-0.26
	M <sub>3</sub>	0.87	-0.01	-0.08	-0.27	-0.21
	M <sub>4</sub>	0.90	-0.38	-0.26	-0.34	-0.06
	M <sub>5</sub>	0.83	-0.35	-0.41	-0.30	-0.05
	N <sub>1</sub>	-0.08	-0.06	-0.06	-0.05	-0.06
	N <sub>2</sub>	-0.05	-0.15	-0.14	-0.12	-0.08
	N <sub>3</sub>	-0.12	-0.11	-0.12	-0.09	-0.06
	N <sub>4</sub>	-0.26	-0.24	-0.16	-0.11	-0.02
	N <sub>5</sub>	-0.26	-0.23	-0.23	-0.10	-0.01
	N <sub>6</sub>	0.04	0.05	0.05	0.02	0.01
	N <sub>7</sub>	0.04	0.05	0.03	0.02	0.01
O	K	-0.26	-0.03	-0.03	0.00	0.00

TABLE IV: CVS-EOM-CCSD core ionization potentials (in eV) for  $\text{UO}_2^{2+}$  using uncontracted Dyall double-zeta basis set for all atoms from a calculation in which all orbitals are included in the correlation space.

Atom	Assignment	$^4\text{DC}$	$^4\text{DC}^\dagger$	$^4\text{DC}(\text{SS} \text{SS})$	$^4\text{DC}(\text{SS} \text{SS})^\dagger$
U	K	116535.49	115771.72	116468.28	115704.50
	L <sub>1</sub>	21971.78	21866.51	21959.27	21853.99
	L <sub>2</sub>	21166.06	21058.71	21148.10	21040.75
	L <sub>3</sub>	17322.46	17257.86	17316.74	17252.15
		17322.73	17258.13	17316.74	17252.15
	M <sub>1</sub>	5647.98	5625.90	5644.72	5622.64
	M <sub>2</sub>	5281.17	5259.74	5277.09	5255.66
	M <sub>3</sub>	4386.47	4373.71	4384.83	4372.07
		4386.74	4373.98	4385.38	4372.62
	M <sub>4</sub>	3806.59	3798.56	3805.23	3797.20
		3806.86	3798.83	3805.50	3797.47
	M <sub>5</sub>	3625.91	3620.56	3625.64	3620.29
		3625.91	3620.56	3625.64	3620.29
		3626.18	3620.84	3625.91	3620.56
	N <sub>1</sub>	1501.52	1496.15	1500.70	1495.33
	N <sub>2</sub>	1334.99	1330.01	1333.90	1328.92
	N <sub>3</sub>	1098.52	1095.81	1097.98	1095.26
		1099.07	1096.35	1098.79	1096.08
	N <sub>4</sub>	831.58	830.23	831.31	829.96
		832.12	830.78	831.85	830.51
	N <sub>5</sub>	787.50	786.82	787.50	786.82
		787.77	787.09	787.77	787.09
		788.31	787.64	788.31	787.64

$^\dagger$  Plus QED+Breit contributions from Koziol and Aucar<sup>5</sup>

TABLE V: The difference in CVS-EOM-CCSD core ionization potentials (in eV) for  $\text{UO}_2^{2+(a)}$ ,  $\text{UO}_2^{2+}$  @ 4  $\text{Cl}^-$  and the estimated value for the  $\text{Cs}_2\text{UO}_2\text{Cl}_4$  crystal with the values reported in refs.<sup>1,2,4</sup>. These calculations were performed using uncontracted Dyall

<sup>(a)</sup>double- and <sup>(b)</sup>triple-zeta basis set for all atoms.

Atom Assignment		$\text{UO}_2^{2+}$				$\text{UO}_2^{2+}$ @ 4 $\text{Cl}^-$		$\text{Cs}_2\text{UO}_2\text{Cl}_4$	
		$^4\text{DC}$	$^4\text{DC}^\dagger$	$^4\text{DC}(\text{SS} \text{SS})$	$^4\text{DC}(\text{SS} \text{SS})^\dagger$	$^4\text{DC}$	$^4\text{DC}^\dagger$	$^4\text{DC}$	$^4\text{DC}^\dagger$
U	K	929.49	165.72	862.28	98.50				
	L <sub>1</sub>	214.78	109.51	202.27	96.99				
	L <sub>2</sub>	218.06	110.71	200.10	92.75				
	L <sub>3</sub>	156.46	91.86	150.74	86.15				
		156.73	92.13	150.74	86.15				
	M <sub>1</sub>	99.98	77.90	96.72	74.64				
	M <sub>2</sub>	99.17	77.74	95.09	73.66				
	M <sub>3</sub>	83.47	70.71	81.83	69.07				
		83.74	70.98	82.38	69.62				
	M <sub>4</sub>	78.59	70.56	77.23	69.20	17.25	9.21	22.25	14.21
		78.86	70.83	77.50	69.47	17.03	8.99	22.03	13.99
	M <sub>5</sub>	73.91	68.56	73.64	68.29	12.77	7.43	17.77	12.43
		73.91	68.56	73.64	68.29	12.51	7.17	17.51	12.17
		74.18	68.84	73.91	68.56	12.40	7.05	17.40	12.05
	N <sub>1</sub>	62.52	57.15	61.70	56.33	21.50	16.13	26.50	21.13
	N <sub>2</sub>	63.99	59.01	62.90	57.92	21.85	16.87	26.85	21.87
	N <sub>3</sub>	55.52	52.81	54.98	52.26	15.80	13.08	20.80	18.08
		56.07	53.35	55.79	53.08	14.90	12.18	19.90	17.18
	N <sub>4</sub>	53.28	51.93	53.01	51.66	13.45	12.11	18.45	17.11
		53.82	52.48	53.55	52.21	12.65	11.30	17.65	16.30
	N <sub>5</sub>	51.30	50.62	51.30	50.62	11.98	11.31	16.98	16.31
		51.57	50.89	51.57	50.89	11.31	10.63	16.31	15.63
		52.11	51.44	52.11	51.44	10.89	10.21	15.89	15.21

<sup>†</sup> Plus QED+Breit contributions from Koziol and Aucar<sup>5</sup>

## REFERENCES

- <sup>1</sup>Bearden, J. A. and Burr, A., “Reevaluation of x-ray atomic energy levels,” *Reviews of Modern Physics* **39**, 125 (1967).
- <sup>2</sup>Cardona, M. and Ley, L., *Photoemission in solids I*, Vol. 26 (1978).
- <sup>3</sup>Denning, R., Green, J., Hutchings, T., Dallera, C., Tagliaferri, A., Giarda, K., Brookes, N., and Braicovich, L., “Covalency in the uranyl ion: A polarized x-ray spectroscopic study,” *The Journal of Chemical Physics* **117**, 8008–8020 (2002).
- <sup>4</sup>Fuggle, J. C. and Mårtensson, N., “Core-level binding energies in metals,” *Journal of Electron Spectroscopy and Related Phenomena* **21**, 275–281 (1980).
- <sup>5</sup>Kozioł, K. and Aucar, G. A., “Qed effects on individual atomic orbital energies,” *The Journal of Chemical Physics* **148**, 134101 (2018).
- <sup>6</sup>Vitova, T., Green, J. C., Denning, R. G., Löble, M., Kvashnina, K., Kas, J. J., Jorissen, K., Rehr, J. J., Malcherek, T., and Denecke, M. A., “Polarization dependent high energy resolution x-ray absorption study of dicesium uranyl tetrachloride,” *Inorganic chemistry* **54**, 174–182 (2015).